AG NANO-DENDRITIC THREE-DIMENSIONAL (3D) SURFACE-ENHANCED RAMAN SCATTERING (SERS) SUBSTRATE FOR IN-SITU LIQUID MEDIA DETECTION

by

MILIND MANSING PAWAR

Presented to the Faculty of the Graduate School of

The University of Texas at Arlington in Partial Fulfillment

of the Requirements

for the Degree of

MASTER OF SCIENCE IN MATERIALS SCIENCE AND ENGINEERING

THE UNIVERSITY OF TEXAS AT ARLINGTON

May 2017

Acknowledgements

I would like to thank each and every person who were extremely helpful during my graduate studies. I cannot think of my graduate study to be accomplished without support of my “Guru” Dr. Yaowu Hao whose constant support and advise shaped this thesis. His excellent knowledge and creativity were immense source of inspiration and led me to develop more and more interest towards science. It was Dr. Hao who made me believe in my work and shaped this research.

My special thanks to Dr. Efstathios "Stathis" I. Meletis and Dr. Pelagia Irene (Perena) Gouma to be a part of thesis dissertation committee. In addition to this, I would like to acknowledge all MSE faculty members for providing better insight towards materials science and engineering. Ms. Beth Robinson and Ms. Jennifer Standlee were always there for administrative requirements. I would also like to thank Dr. J. Jiang and David Yan for their support for materials characterization at UTA.

I have been delighted to having worked with great team members, Muddasir, Aaron, Aseem, Anadi, Chris, Prajwal, Francis, Sina and Yash in the Metal nanostructure research group in the MSE department. I would also like to thank my friends Marg, Tarun, Tirth, Ninad, Abhishek, Himanshu, Urvil and Himat. At the end, I am honored and privileged to have a wonderful family. I thank my parents, Mansing Rajaram Pawar and Sheela Pawar, my sister Bhumika Pawar for their unconditional love and encouragement.

May 17, 2017

Abstract

AG NANO-DENDRITIC THREE-DIMENSIONAL (3D) SURFACE-ENHANCED RAMAN SCATTERING (SERS) SUBSTRATE FOR IN-SITU LIQUID MEDIA DETECTION

Milind Mansing Pawar, MS

The University of Texas at Arlington, 2017

Supervising Professor: Yaowu Hao

Continuous monitoring of certain environmental pollutants, biological species, chemical species, and explosives are of utmost importance in recent times. Surface-enhanced Raman scattering (SERS) provides most promising option as it is a highly sensitive technique which allows for ultrasensitive detection of molecules and provides excellent structural information. To obtain rich results through Surface-enhanced Raman scattering, proper design of enhancing substrate plays vital role. Contemporary SERS substrates don't provide ease to detect liquid analytes for in-situ spectroscopy. Liquid media detection through SERS relies on highly statistical binding of analytes to SERS-sensitive hot spots. Moreover, it becomes extremely difficult to detect flowing liquid media in-situ with two-dimensional substrates as very small volume of Liquid contact with substrates. Single crystal Ag dendrite structures possess high surface area along with narrow gaps and sharp edges. Compared with other nanostructures, the hierarchical nanostructures-dendritic Ag, consisting of multi-level branches can significantly promote the SERS enhancement and serve as effective SERS substrates with high sensitivity and reproducibility. Such complex nanostructures may provide a large amount of "hot spots" at the end of branches or the junctions of adjacent Ag branches. In addition, the large surface area of Ag dendrites can enhance the interaction between analytes and sensing substrates. Ag dendrites can easily

be produced, by use of one of the simplest galvanic reactions, the reaction of $AgNO_3$ with Cu. We have developed novel yet simple Surface-enhanced Raman scattering- active substrate having three-dimensional array of Ag-dendrites grown within square geometry capillary tube of borosilicate glass via such galvanic replacement reaction with inserted copper wire. Systematic study of growth mechanism of Ag-dendrites was carried out and complex nature of seemingly “simple” galvanic replacement reaction has been proposed. The resultant Ag dendrites were characterized by scanning electron microscopy, transmission electron microscopy, energy dispersive spectroscopy and X-ray diffraction. A time-dependent investigation on the growth mechanism of the Ag dendrites revealed that they develop through a particle-mediated growth process. The effect of the reactant concentrations on the morphology of the synthesized Ag dendrites was also studied. This study on Ag dendrite growth mechanisms are not only scientifically intriguing, but also technologically important. Novel Ag dendrite three-dimensional SERS substrate exhibits excellent sensitivity and a very good reproducibility. We have detected rhodamine 6G (R6G) with lowest concentration of 10^{-11} M in aqueous solution. These Ag dendrite nanostructured three-dimensional SERS substrates are proved as excellent in-situ liquid media Raman detection substrates due to availability of extensive hot spots. It has significant potential to be used as SERS substrates for fast and accurate detection of trace amount of organic contaminants in flowing liquid media.

Keywords: Surface-enhanced Raman scattering, Ultrasensitive detection, Ag dendrite three-dimensional SERS substrate, Galvanic replacement reaction, Particle mediated growth process.

Table of Contents

List of Illustrations

List of Tables

Chapter 1

Introduction

Raman spectroscopy is an analytical tool to decipher the vibrational modes of molecular structures [1-3]. Cross sections that emits Raman scattering are usually of the order of 10^{-30} cm^2 $molecule^{-1}$ sr^{-1}, in addition to that very low sensitivity makes it almost impossible to detect low concentrations [1]. “Sensitivity” is the principal shortcoming of Raman spectroscopy, which can be overcome through surface enhanced Raman scattering mechanism [4]. Surface-enhanced Raman scattering (SERS) is a surface sensitive widely used for many biological, chemical, and environmental applications. Rich structural information can be obtained without any sample preparation and as low as single molecule can be detected theoretically [5-8]. SERS techniques have similar advantages of Raman spectroscopy which includes low background signals [9], specific signal for particular molecule [10]. share the advantages of conventional Raman spectroscopy, such as the narrow signal bandwidth giving low background and multiplexing capability [9], with the diversity of molecular vibration allowing for high specificity of SERS signal [10]. Additionally, it is a non-destructive technology due to no sample preparation and destruction for SERS.

Detection of analytes with particular specificity as well as very high sensitivity in flowing liquid media is of essential importance to monitor certain environmental pollutant, explosive materials, chemical agents, and pharmaceutical drugs [11-13]. SERS substrate can be used for continuous monitoring of such flowing liquid media. However, one of the important limitation of SERS application for practical purposes is statistical bonding of analyte to surface of SERS hot spot [14-18]. Hence, it becomes extremely challenging to detect highly diluted solutions in-situ.

To overcome above mentioned problem, design and development of robust SERS substrate becomes more important. Uniform surface, high reproducibility and low cost are some of the features that substrate should have. Noble metals show excellent plasmonic activities such as excellent electrical conductivity as well as localized surface plasmon resonance (LSPR) properties makes Ag nanostructures excellent candidate for SERS substrate. Silver nanostructures in the form of nanowires [19], nanoprisms [20], flower-like particles [21], nanosheet-assembled micro-hemispheres [22], nanorod arrays [23] can be explored for SERS.

The hierarchical nanostructures-dendritic Ag, contains multi banched structure which can increase the SERS enhancement, provide more surface for high sensitivity and better results. We can expect that because of complex structure, highly dense hot spots can be created at the tip of these branches as well as at the junctions [24]. Moreover. High surface area of dendritic structure can also provide more interaction of nanostructure and analyte by high adsorption possibility. Many capable dendritic Ag structures-based SERS substrates have been developed and utilized for liquid media detection. However, SERS substrates prepared with hierarchical Ag nanostructures are still form 2D array and require evaporation of solvent. Two-dimensional array of hierarchical structures is not compatible to monitor flowing liquid media.

As of today, numerous Ag hierarchical nanostructures with diverse structural features and applications have been fabricated through different synthesis methods including electrochemical deposition [25-41], γ-irradiated deposition, electroless redox reaction [42-58], wet chemical route using reducing agents in aqueous solution [59-72], photocatalytic reduction [73,74], decomposition by visible light irradiation [75], ultraviolet irradiation of surfactant micelles [76], ultrasonically assisted templated synthesis, iodination treatment to the evaporated Ag foil surface [77], sono-electrochemical deposition

[78-81], and photoreduction by ultraviolet irradiation [82]. However, each of the mentioned methods are inflicted to a degree by some deficiencies, such as requiring special equipment, time consuming (up to 30 days), impurity, using highly hazardous materials (e.g. HF), needs of seed particles and templates, multiple capping agents, multiple synthetic steps, problems associated with removal of templates or surfactants from the surface of the Ag nanostructure products, high-cost or low-yield restrictions, and poor reproducibility, to name a few.

Among all the above synthesis methods galvanic replacement is the simple and attractive method to fabricate varied nanostructures of noble metals (such as Au, Ag, Pd, and Pt) and their alloys. Galvanic replacement reaction is thermodynamically driven by a favorable difference between reduction potentials of the deposited metal and the sacrificial material. The Galvanic replacement method is very effective way to make MNPs due to its ability to tune the size and shape, and to change the composition, morphology of the resultant nanostructures. Although the main governing principle of galvanic replacement is very straightforward, controlling the morphology and structure of produced nanostructures have not been that easy in all cases, as they are very sensitive to the synthesis condition.

In most of these studies, galvanic replacement (redox reaction) and Ag dendrite growth generally occurred through the direct electron transfer between Ag^{+} and the sacrificial substrate, leading to the formation of Ag hierarchical structures onto the surface of the substrate or into the template containing the sacrificial material. The diffusion-limited aggregation (DLA) model and the anisotropic crystal growth were used to explain the growth of Ag nano-dendrites. The dendrite nanostructure growth by the galvanic replacement reaction (GRR) process is dependent on the thermodynamic factors and the inherent crystal structure of the material. At the beginning of this reaction, GRR will instantly initiated at the highest surface energy spots where the surface is rough (defects, stacking

fault or steps) and the bulk energy of the total system tends to decline. Thus, Ag particles aggregate dendritic rather than a thermodynamically stable hexagonal structure. Consequently, some byproducts (like smaller Ag nanoparticles) could form and mix with the Ag dendrites or special care must be taken to detach the dendrites from the substrates/templates. GRR is a facile, low-cost, and simple synthesis process for large-scale.

In this research study, innovative design of three-dimensional complex network Ag dendrite SERS substrate with excellent enhancement properties has been developed. Robust SERS substrate showed consistent, rapid, and reproducible SERS results. “Simple” galvanic replacement reaction was used to prepare economical and fast production of SERS substrate for in-situ liquid media detection. Interestingly, when we tried to use this “simple” reaction to form Ag dendrites inside the channels (about 300 nm) of anodic aluminum oxide (AAO) membranes by depositing Cu at one end to cover the channels and adding $AgNO_3$ solution into the membranes, a large amount of well-defined Ag dendrites was observed on the top surface of AAO membrane without any direct connection to Cu layer at the bottom. We conducted a series of experiments to explain this surprising result, and proposed a new reaction and Ag dendrite formation mechanism.

Chapter 2

Background

2.1 Raman Scattering Theory

Scattering is an interaction of electromagnetic (EM) wave with material. When EM wave with frequency v_0 interact with a material, molecules start to perturb periodically under influence of EM wave. This perturbation of electron cloud creates induced dipole moment (P). Such oscillating induced dipole moment act as a source of EM radiation which result into scattered radiation. Major portion of this scattered light has exact frequency as incident light frequency (v_0), which is known as elastic scattering or Raleigh scattering. However, very small portion of scattered light having different frequency than incident light is referred as inelastic scattering of Raman scattering [83].

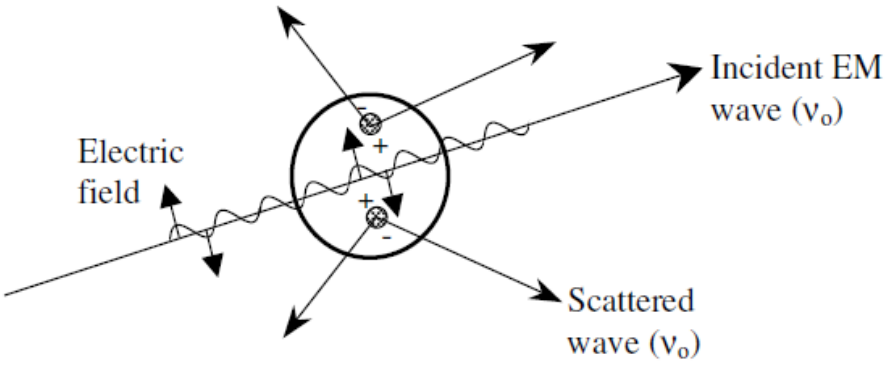

1 Interaction of Electromagnetic wave with material [83]

Strength of induced dipole moment (P) is proportional to electric field, and the proportionality is called polarizability, as given by

$$P = \alpha \bar{E} \tag{1}$$

where α is the polarizability and $\bar{E}$ is the strength of electric field of the incident EM wave. Molecular structure and nature of bonds determine the polarizability of a material. Time dependent electric field of the incident EM wave, may be expressed as

$$\bar{E} = E_0 \cos(2\pi v_0 t) \tag{2}$$

where v_0 is the frequency (Hz) of the incident EM ($v = \frac{c}{\lambda}$). Substituting Eqn. (2) into (1) yields the time-dependent induced dipole moment,

$$P = \alpha E_0 \cos(2\pi v_0 t) \tag{3}$$

As the ability to perturb electron cloud is dependent on the position of atoms, polarizability becomes function of the position. Vibrational energies are quantized in the similar manner as electronic energies. The vibrational energy of any particular mode can be represented by,

$$E_0 = \left(j + {}^1/_2\right) h v_{vib} \tag{4}$$

where j is the vibrational quantum number ($j = 0,1,2 \ldots$), v_{vib} is the frequency of the vibrational mode, and h is the Planck constant. The particular vibrational mode displacement dQ of the atoms about their equilibrium position can be expressed as

$$dQ = Q_0 \cos(2\pi v_{vib} t) \tag{5}$$

where Q_0 is the maximum displacement about the equilibrium position. Taylor series expansion can be considered for smaller displacements, and its second and more order differentiation term can be ignored.

$$\alpha = \alpha_0 + \frac{\partial \alpha}{\partial Q} dQ \tag{6}$$

where α_o is the polarizability of the molecular mode at equilibrium position. Substituting eqn 5 in eqn 6 yields following eqn 7.

$$\alpha = \alpha_0 + \frac{\partial \alpha}{\partial Q} Q_0 \cos(2\pi v_{vib} t) \tag{7}$$

Finally, Eqn. (7) may be substituted into Eqn. (3), which yield

$$P = \alpha_0 E_0 \cos(2\pi v_0 t) + \frac{\partial \alpha}{\partial Q} Q_0 E_0 \cos(2\pi v_0 t) \cos(2\pi v_{vib} t) \tag{8}$$

By using a trigonometric identity, above equation can be rewrite as,

$$P = \alpha_0 E_0 \cos(2\pi v_0 t) + \frac{\partial \alpha}{\partial Q} \frac{Q_0 E_0}{2} \{\cos(2\pi (v_0 - v_{vib}) t) + \cos(2\pi (v_0 + v_{vib}) t)\} \tag{9}$$

The above equation suggests that induced dipole moments are created at three different frequencies, namely v_0, $(v_0 - v_{vib})$, and $(v_0 + v_{vib})$, which in return produce scattered radiation at these same three frequencies. The first scattered frequency represents elastic scattering as it has same frequency as incident light. However, the latter two frequencies are considered to be inelastic because of their shifts. These latter two cases are considered as Raman scattering, with the down-shifted frequency known as Stokes scattering, and the up-shifted frequency known as anti-Stokes scattering.

It should be noted from the final equation that the necessary condition for Raman scattering, the term $\frac{\partial \alpha}{\partial Q}$ must be non-zero. Physical interpretation of this term suggests that the vibrational displacement of atoms corresponding to a vibrational mode causes change in the polarizability. Let's consider a diatomic molecule A-B, with maximum vibrational displacement Q_0, as shown below

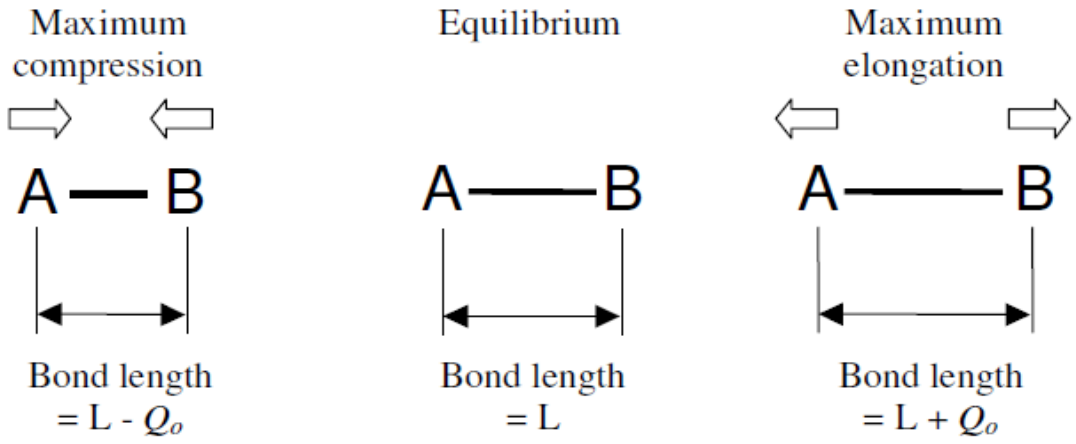

2 Vibrational displacement of A-B about the equilibrium position [83].

From figure 2, it can be considered that when A-B are in maximum compression, their electrons will have attraction from nucleus of other atom and hence it will be very difficult to perturb electrons in this situation. Here polarizability will be minimum. On the

contrary when atoms A-B are at maximum distance apart, electrons can be easily perturbed in this situation. Hence polarizability will be highest in this situation. However, one should note here that polarizability is continuously changing with respect to displacement and we can draw a plot for it which look as below.

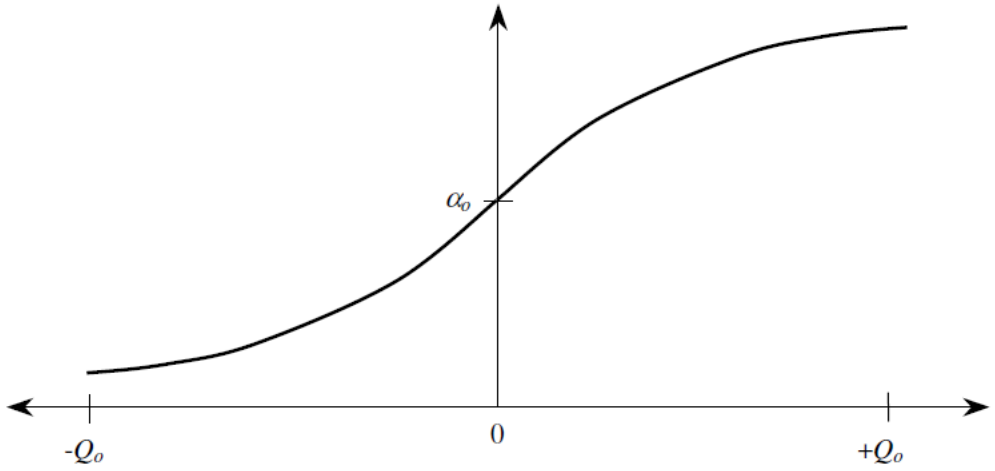

3 Polarizability of A-B as a function of vibrational displacement about equilibrium [83].

In above plot $\frac{\partial \alpha}{\partial Q}$ is non-zero though out the range and full-fill the Raman condition. Hence it should produce Raman scattering at the two frequencies $(v_0 - v_{vib})$ and $(v_0 + v_{vib})$. [83]

2.2 Raman Spectroscopy

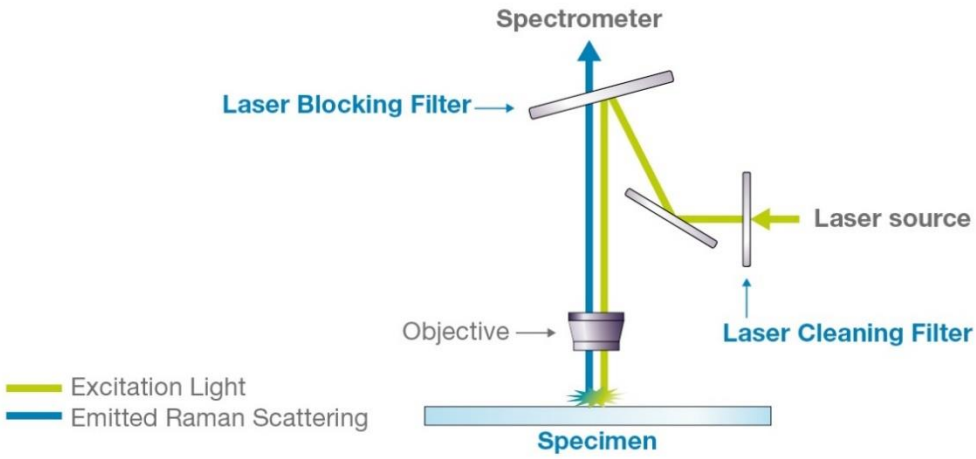

4 Schematic diagram of Raman spectrometer (adopted from Raman Filters - Optical Filters for Raman Spectroscopy. (n.d.)., from https://www.opticsbalzers.com/en/products/filters/raman-filters.html)

Raman microscopes are a commonly used tool for material characterization. Raman microscopes can examine microscopic area of material by illuminated laser beam down to the micrometer level. This tool should be referred to as Raman micro spectroscope because Raman microscope is not primarily used for imaging purposes. Typical Raman microscope includes the following elements [132]:

1. Laser source
2. Illumination and collection system
3. Spectral analyzer

4. Detection and computer control system

Raman spectroscope needs to use highly monochromatic light illuminating to the sample, which can be provided by the laser source. Laser source usually used are gas continuous wave lasers for example Ar, Kr and He-Ne [132]. These laser sources are able to generate beams with different wavelengths. Also, the laser source can easily generate several tens of mW of laser power. A filter can be used to make laser beam monochromatic. The microscope can collect the Raman scattered light reflected from the sample surface. This scattered light will travel to the detector. Inelastic scattering of lights generate Raman scattering which is very weak in terms of intensity. In order to eliminate elastically scattered light, the light from the microscope has to pass through a special filter before the light reaches the analyzer.

The important component of the spectral analyzer in the system is diffracting grating. It is used to disperse Raman scattered light depending on the wavenumbers of light. There are some fine parallel grooves on the surface of the diffraction grating that are used to equally dispersed wavenumbers of light. When the light shines the diffraction grating, the grating disperses the light with discrete direction.

The detector is used to record different wavelengths of Raman scattered light. It is made from photoelectric materials. The detector is able to convert photon signals to electric signals. The most commonly used detector is a charge-coupled device (CCD) detector. A CCD detector is made from 19 silicon-based semiconductor photosensitive elements. It can record and detect intensity of different wavelengths distributed by the diffraction grating. The computer is used to calculate and plot the Raman shift versus wavenumber for the Raman spectrum.

The biggest limitation of Raman spectroscopy is a fluorescence problem due to the fact colored samples and impurities might absorb laser radiation and emit it again as

fluorescence. The intensity of fluorescence can be as much as 10000 times higher than Raman scattered light. Hence, the intensity of fluorescence signal might cover the Raman scattered signal completely. Three methods can be used to minimize fluorescence [132]:

1. Illuminating the material using high-power laser beam with prolonged time can make the impurity fluorescence bleached out.
2. Changing the wavelength of laser excitation a longer wavelength.
3. An electron gate can be used to measure the Raman signal. Because Raman scattering lifetime is much shorter than fluorescence.

2.3 Surface-enhanced Raman Scattering (SERS)

Fleischman et al. in 1974 [84] were to be first to observe Surface-enhanced Raman scattering (SERS), and later discovered by *Jeanmarie* and *Van Duyne* [85] and *Albrecht* and *Creighton* [86] in 1977 [81]. Here observation was considered because of increased surface area of roughened silver electrode [81][131]. Martin Moskovits first proposed that unusual increase in Raman cross section was because of the presence of excited surface plasmons [87][81]. In the last two decades, significant progress has been reported in the field of SERS as it was reported that enough SERS intensity can be obtained to detect a single molecule [88-99].

2.3.1 Mechanism of SERS

Various mechanisms were proposed to understand translation of surface plasmon to SERS. Amongst several proposed mechanisms, electromagnetic enhancement model was simultaneously presented in 1980 by Gersten [100, 101, 131], Gersten and Nitzan

[102, 103] and McCall et al. [104, 105] and extended by Kerker et al. [106,107, 108, 109,110, 131].

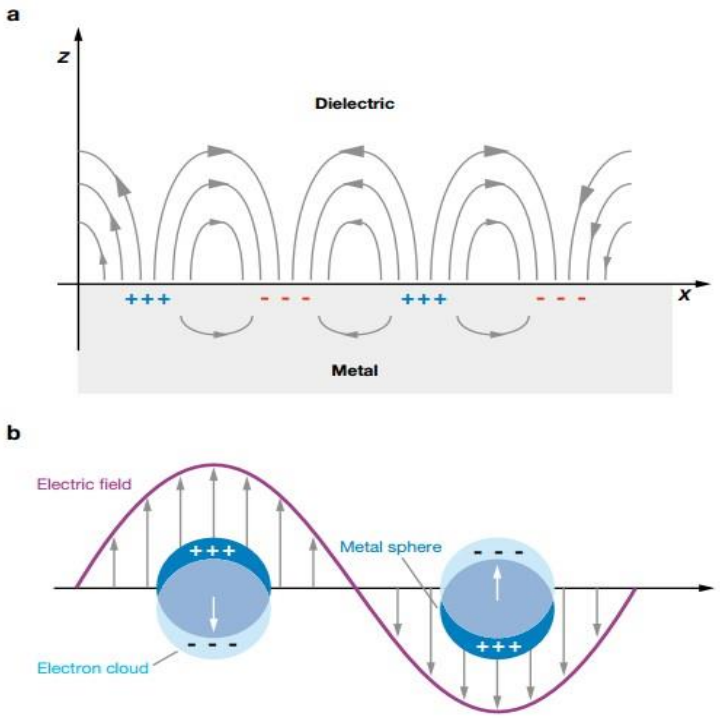

5 a. Surface Plasmon b. Localized Surface Plasmon (adopted from Willets, K. A., & Van Duyne, R. P. (2007). Localized surface plasmon resonance spectroscopy and sensing. Annu. Rev. Phys. Chem., 58, 267-297.)

Collective oscillations of the conduction electrons leaving behind ionic metal cores are called surface plasmon [111]. When particle is much smaller than excitation light's wavelength, dipolar plasmon pays important role [131]. Systems having high conductivity can sustain such excitations because of free electrons. Free electrons can produce more sharp and intense dipolar plasmon resonance. Light of characteristic wavelength radiates when the excitation light is in resonance with the dipolar plasmon [112][131]. Produced radiation is separate from the excitation light and for certain area of nanoparticle light can be amplified and in certain part it will be depleted.

Due to weak effect of Raman scattering, if analyte molecules are adsorbed on a plasmonic nanoparticle surface, such weak Raman scattering signal can be drastically enhanced. This effect of enhancement is known as surface-enhanced Raman scattering (SERS). In certain cases, such enhancement is 10^{14}-10^{15} order and it can detect a single molecule. Complex nature of SERS enhancement mechanism is can be explained by (i) chemical enhancement, (ii) resonance Raman enhancement, (iii) charge-transfer resonance enhancement, and (iv) plasmon resonance enhancement processes [113]. Plasmon resonance enhancement is considered to be the largest to the observed SERS signal, and it can also be referred as the electromagnetic (EM) enhancement mechanism.

2.3.2 The Electromagnetic Enhancement

Huge electromagnetic enhancement of Raman scattering from molecules occurs interacting metal nanoparticles, for example Ag or gold nanoparticles, in vicinity. If metal particles are radiated with light having wavelength compatible to induce LSPR then the EM enhancement is very strong. LSPR of the nanoparticle depends upon many factors such as the particle size, shape, and surrounding medium. Presence of other nanoparticles nearby with inter-particle interaction can affect the LSPR ("hot spots") [114].

Electromagnetic enhancement model for SERS is represented in Figure 6. The incident light can induce dipole moment in molecule as well as nanoparticles hence two sources of dipole fields are available. Here, a molecule is adjacent to a nanoparticle so that coupling of dipole field can be expected. It is easy for us to visualize this as two processes occurring at the same time [114].

At the beginning the incident electromagnetic field, E_0, excites the particle localized surface plasmon and induce oscillating dipole moment,

$$P = \alpha_p E_0 \quad (10)$$

where α_p is the particle polarizability (generally a tensor). Huge local fields $E_{0,loc}$ generated by the induced particle polarization, hence the incident field is also enhanced yielding $(E_0 + E_{0,loc})$. This total field excites the analyte molecule which can emit Raman scattering. The incident light intensity is then proportional to $(E_0 + E_{0,loc})^2$.

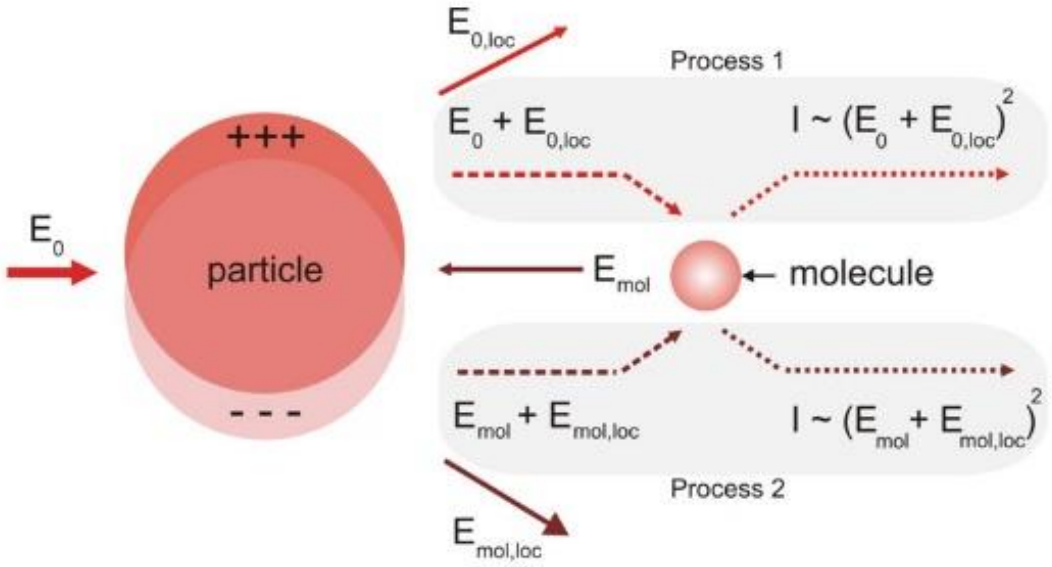

6 Schematic representation of SERS electromagnetic enhancement [114]

Now let's consider same scenario for the molecule. The emitted field from a molecule, E_{mol}, is also enhanced by a metal particle giving total filed of $(E_{mol} + E_{mol,loc})$. The Raman intensity is now $I \sim (E_{mol} + E_{mol,loc})^2$. Therefore, the Raman signal is enhanced by E^2 at every stage.

The dipole moments of a particle and a molecule can be expressed as follows:

$$p = \alpha_p E_0 \tag{11}$$

$$m = \alpha_m E_0 \tag{12}$$

Where E_0 is the incident field, α_p and α_m are the particle and molecule polarizabilities, respectively. As analyte molecule is adjacent to nanoparticle surface, the particle dipole field ($E_p = Cp$) can be added to the incident field for the calculation of the dipole moment of the molecule (C is a constant). Similarly, the dipole field from the molecule ($E_m = Cm$) can be added to the incident field when defining the dipole moment for the particle.

The coupled dipole system becomes:

$$p = \alpha_p(E_0 + Cm) \tag{13}$$

$$m = \alpha_m(E_0 + Cp) \tag{14}$$

Solving the system yields

$$p = \alpha_p \frac{1 + C\alpha_m}{1 - C^2\alpha_p\alpha_m} E_0 = \alpha_p^o E_0 \tag{15}$$

$$m = \alpha_m \frac{1 + C\alpha_p}{1 - C^2\alpha_p\alpha_m} E_0 = \alpha_m^o E_0 \tag{16}$$

Near the particle LSPR α_p >> α_m and the effective particle polarizability α_p^o will dominate the system. Due to the contribution from α_m the polarizability can be modified.

SERS electromagnetic enhancement factor is defined as,

$$G = \frac{I_{SERS}}{I_{Raman}} \tag{17}$$

$$\frac{I_{SERS}}{I_{Raman}} = \left[\frac{C\alpha_p + C^2\alpha_p^2}{(1 - C^2\alpha_p\alpha_m)^2}\right]^2 \approx (C\alpha_p)^4 \approx \left|\frac{E_{loc}}{E_0}\right|^4 \tag{18}$$

Therefore, the 4th power of the ratio between the field near the nanoparticle and the incident field can be achieved [114].

SERS can be considered truly as nanoscience because in order to achieve surface enhancement of light, metal particle should be smaller than the wavelength of excitation source [131]. SERS-active systems have feature in the range of 5 nm to 100 nm. Similarly, SERS active structure's dimensions cannot be smaller than analyte molecule. Wavelength determines the upper dimensional limit of the SERS-active system. If nanostructures having features dimensions more than the wavelength of excitation light, it cannot generate dipolar plasmon which is responsible for SERS. For the lower dimensional limit, if nanostructures become too small, conductivity of the metal nanoparticles reduce drastically because of occurring of electronic scattering at the particle's surface [115, 116, 117]. In response, reradiated field reduced in strength as well as the quality of dipolar resonance.

2.3.3 Interacting Nanostructures (Hotspots):

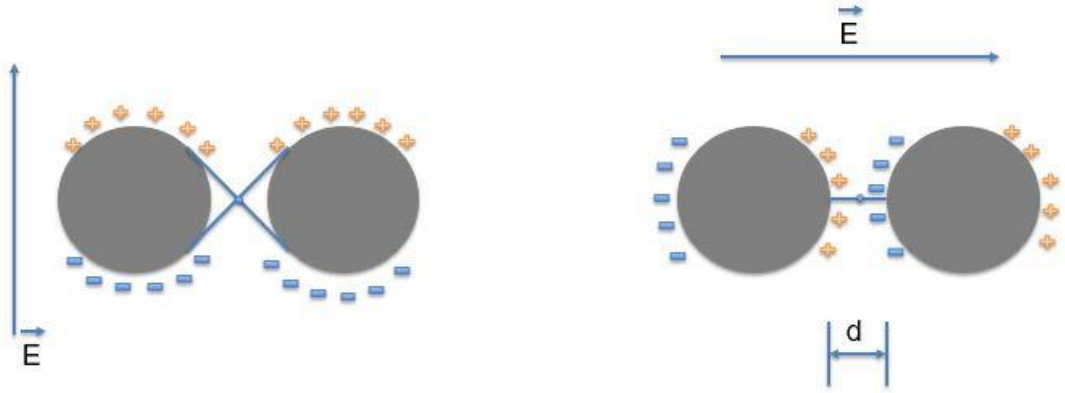

7 Effect of orientation of vector-E with respect to hotspots [81]

Effective SERS-active systems contain interacting nanoparticles, nanostructures or nanofeatures. Such SERS active systems such as either particles or cavities satisfy dual advantage of providing high field enhancement with better control of SERS platforms [118, 119, 120]. Raman enhancement of ~ 10^{10} can be achieved for molecules localized within confined volume of nano features [121, 122, 123, 124]. If two nanoparticles are placed within ~ 1nm or less with appropriate excitation light source, if electric field is aligned with axis connecting nanoparticles can result into very high enhancement. Such a massive enhancement reduces dramatically if distance between these particle increases. It should also be noted that if light source having electric field aligned across the axis connecting nanoparticles, then enhancement has no significant effect (figure 7).

Referring to figure 7, a molecule located in the interstice between two metal nanoparticles is under influence of two sets of charges because of individual polarization of nanoparticles. As we reduce the distance between nanoparticles, the capacitive field sensed by the molecule increased drastically. Increment in the enhancement can be approximated as d^{-8} where d is the gap size between the two nanowires [81][131]. On the

other side, if polarization of light is as shown in figure 7 on left, it will not increase the enhancement. Moreover, in this situation even if the distance between nanoparticles is reduced, no significant enhancement can be observed.

2.4 Ag nanostructures and their SERS application

Novel applications and intriguing properties of metal nanostructures have drawn significant attention. Among different metal nanostructures, the Ag (Ag) nanostructure has been extensively studied due to its unique electrical, chemical, and optical properties. Properties of such Ag nanostructures can be tuned by simply changing their size and shape, as a result, a variety of methods have been demonstrated to provide shape-controlled synthesis of Ag nanostructures. Till date various shapes of Ag nanostructures have been developed such as nanowires, nanodisks, nanoprism, nanorods to name a few. However, among these many shapes Ag dendrites have their unique importance. Ag dendrites are made of major trunks and many hierarchical branches with attached leaves providing high surface area and interfacial structures that largely enhance certain desired features.

A variety of methods to fabricate Ag hierarchical nanostructures with diverse structural features have been employed which include electrochemical deposition [25-41], electroless redox reaction [42-58], wet chemical route using reducing agents in aqueous solution [59-72], photocatalytic reduction [73, 74], decomposition by visible light irradiation [75], ultraviolet irradiation of surfactant micelles [76], ultrasonically assisted templated synthesis, iodination treatment to the evaporated Ag foil surface [77], sono-electrochemical deposition [78-81], and photoreduction by ultraviolet irradiation [82]. However, each of this method have some deficiencies, such as requiring special. equipment, time consuming (up to 30 days), impurity, using highly hazardous materials (e.g. HF), introduction of seed

particles and templates, multiple capping agents, multiple synthetic steps, difficulties to remove the templates or surfactants from the surface of the products, high-cost or low-yield restrictions, and poor reproducibility.

By a considerable extent, wet chemical reaction, electrochemical deposition, and galvanic replacement have been the most commonly used methods for production of Ag fractal nanostructures. Wet chemical technique, as one of the first choices not only for making Ag dendrites but also numerous other metallic nanostructures, is based on the reduction of Ag ions in an aqueous solution using a soluble reducing agent. Nevertheless, in most cases, surfactants and organic/inorganic moieties are inevitable to control aggregation and growth direction. Moreover, the reaction is usually conducted under special condition, requiring vigorous stirring, heating or cooling, and precise adjustment of pH. In contrast, electrochemical deposition method benefits from relatively good control over reduction and growth kinetics by adjusting applied potential, while it lacks the versatility of wet chemical and galvanic replacement techniques to produce diverse more sophisticated nanostructures without introducing more complicated templates and reagents into the reaction process.

2.5 Galvanic Replacement Method:

Among all the above synthesis methods galvanic replacement is the simple and attractive method to fabricate varied nanostructures of noble metals (such as Au, Ag, Pd, and Pt) and their alloys. Galvanic replacement reaction is thermodynamically driven by a favorable difference between reduction potentials of the deposited metal and the sacrificial material. It is an electrochemical process that involves the oxidation of a metal (which is referred as sacrificial templates) by the ions of another metal having higher reduction potential. The Galvanic replacement method is very effective way to make metal

nanoparticles (MNPs) due to its ability to tune the size and shape, and to change the composition, morphology of the resultant nanostructures. Accordingly, even Ag nanoparticles (Ag^{+}/Ag E = 0.8 V vs. SHE) could serve as seeds and reducing agents for synthesis of more noble metal nanostructures such as gold (Au^{3+}/Au E = 1.5 V vs. SHE). Although the main governing principle of galvanic replacement is very straightforward, controlling the morphology and structure of produced nanostructures have not been that easy in all cases, as they are very sensitive to the synthesis condition. The synthesis parameters comprise of ion concentrations, temperature, and the initial state of the sacrificial material.

Recently, the formation of Ag dendrites via galvanic replacement have been reported by several studies using various metals that are more reactive than Ag (e.g. Cu, Mg, Al, Zn, Ni, Sn) as sacrificial substrates. In most of these studies, galvanic replacement (redox reaction) and Ag dendrite growth generally occurred through the direct electron transfer between Ag^{+} and the sacrificial substrate, resulting into the formation of Ag hierarchical structures onto the surface of the substrate or into the template containing the sacrificial material.

The diffusion-limited aggregation (DLA) model and the anisotropic crystal growth were used to explain the growth of Ag nano-dendrites. The dendrite nanostructure growth by the galvanic replacement reaction (GRR) process is dependent on the thermodynamic factors as well as the crystal structure of the material. At the beginning of this reaction, GRR will instantly initiated at the highest surface energy spots where the surface is rough (defects, stacking fault or steps) and decline in the bulk energy of the system can be observed. Thus, Ag particles aggregate into dendritic shape rather than forming a thermodynamically stable hexagonal structure. Consequently, some byproducts (like smaller Ag nanoparticles) could form and mix with the Ag dendrites or special care must

be taken to detach the dendrites from the substrates/templates. GRR is a facile, low-cost, and simple synthesis process for large-scale production.

As one of the simplest galvanic reactions, the reaction of $AgNO_3$ with Cu has indeed been used in high school chemistry class to demonstrate the galvanic reaction and crystal growth. The formation of Ag dendrites can be explained by a simple reaction mechanism as follows.

Reduction reaction first takes place on Cu, and then on newly formed Ag.

$$\mathbf{Ag^+ + e^- \rightarrow Ag},$$

The electron comes from the oxidation reaction, which takes place at Cu surface where Cu^{2+} is released into the solution, and electron transport inside metal to Ag surface to reduce Ag^+.

$$\mathbf{Cu \rightarrow Cu^{2+} + 2e^-},$$

The reduction reaction rate is higher on Ag (111) surface, leading to preferred growth along [111] direction which results in the formation of Ag dendrites.

Interestingly, when we tried to use this simple reaction to form Ag dendrites inside the channels (about 300 nm) of anodic aluminum oxide (AAO) membranes by depositing Cu at one end to cover the channels and adding $AgNO_3$ solution into the membranes, a large amount of well-defined Ag dendrites was observed on the top surface of AAO membrane without any direct connection to Cu layer at the bottom. Such observations contradict partly this formation mechanism, indicating a much more complicated scenario for this simple galvanic reaction. We conducted a series of experiments to explain this surprising result, and proposed a new reaction and Ag dendrite formation mechanism.

Chapter 3: New Insight into Galvanic Replacement Reaction of $AgNO_3$ with Cu

3.1 Introduction

Simple galvanic replacement reaction of $AgNO_3$ with Cu can produce Ag dendritic nanostructures and provides excellent control for its morphology, size, and distribution. However, it has been found that this seemingly simple reaction is actually not that simple. In this section detailed description of complex reaction mechanism and growth mechanism has been proposed through series of experiments.

3.2 Synthesis of Ag dendrites inside AAO Membrane

Chemicals and reagents:

$AgNO_3$ was purchased from Alfa Aesar (Ward Hill, MA, USA). Anodic aluminum oxide (AAO) membranes (Whatman Anodisc Inorganic Filter Membrane, 0.2 µm pore size, 47 mm diameter, supported) were obtained from Sigma-Aldrich (St. Louis, MO, USA). Griess Reagent was also purchased from Sigma-Aldrich (St. Louis, MO, USA). Water used throughout all these experiments was purified with a Millipore system.

Part 1: Ag dendrites on Anodic Aluminum Oxide (AAO) membrane

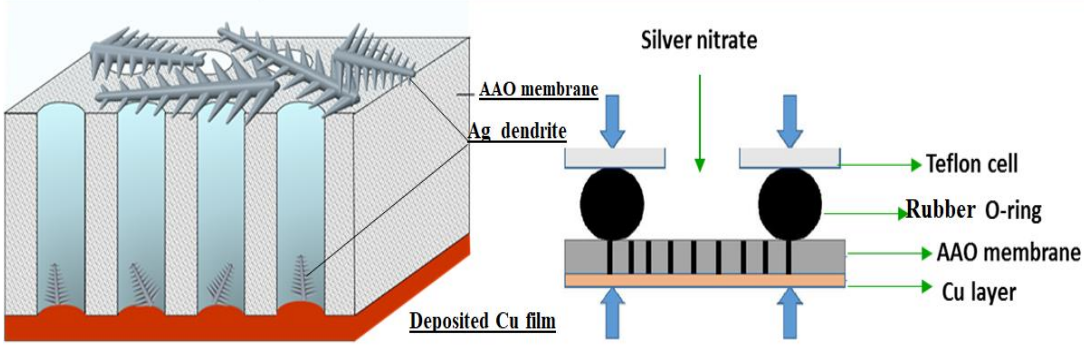

8 Schematic illustration for Ag dendrite formation on AAO membrane

The schematic illustration of the whole experimental setup is depicted in figure 8, in which an anodic aluminum oxide (AAO) membrane was put on a flat surface (silicon wafer), and a sealed Teflon cell with a diameter of ~1cm was placed on the top of the AAO membrane. The bottom side of AAO was deposited with a 500 nm Cu layer by a thermal evaporator (NRC 3117). The deposition rate was set to 4±1 Å/s. 1 ml (unless otherwise was stated) of $AgNO_3$ solution at different concentrations (0.01 to 1 M) was poured into the cell for different reaction times (10 s to 11 hours, the reaction was stopped by pouring out the $AgNO_3$ solution). $AgNO_3$ solution could reach to the Cu surface only through the channels of the AAO membrane. The formed Ag dendrites on the top side of membrane through galvanic replacement reaction were collected and washed with DI water through several cycles of centrifugation at 8000 rpm for 5 min. Same procedure was followed for polycarbonate filter paper instead of AAO membrane by keeping other synthesis condition unchanged.

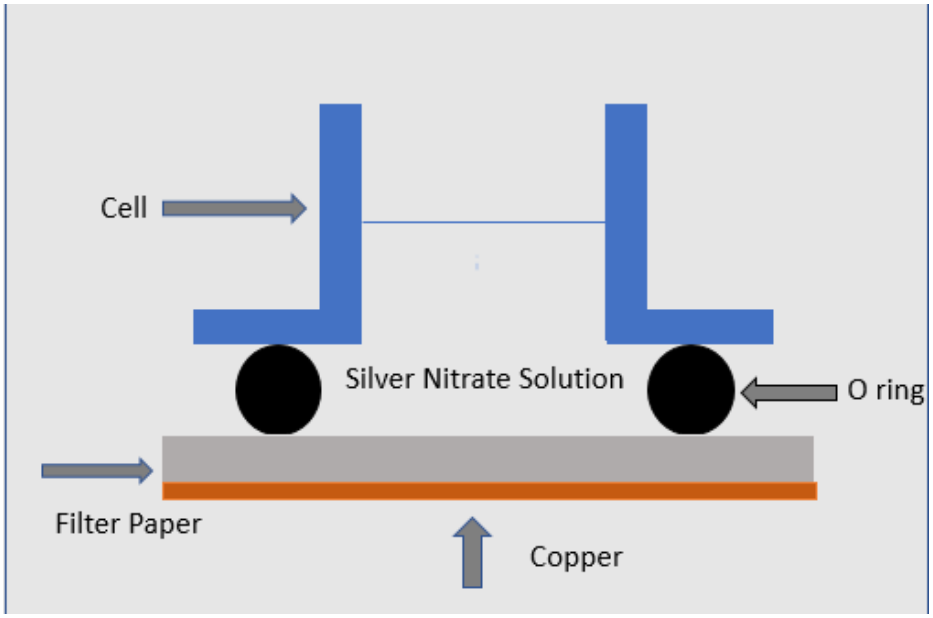

9 Schematic illustration for Ag dendrite formation on filter paper

Figure 9 shows the schematic illustration of another experimental setup, in which filter paper was used instead of AAO membrane, to make sure that AAO membrane was not playing any role in the formation of Ag dendrites on the top side. Surprisingly, identical results were obtained with filter paper as well. In order to make sure that there is proper separation between copper plate and Ag, stacks of filter papers from 2 layers up to 6 layers were used. For all these different cases, same results were obtained i.e. the formation of highly branched Ag dendrites on the top side with no direct contact with copper at the bottom and Ag dendrites at the bottom. The formed Ag dendrites on the top side of membrane were collected and washed with DI water through several cycles of centrifugation at 8000 rpm for 5 min.

3.3 Characterization of Ag Dendrites

Field-emission scanning electron microscopy (FE-SEM, ZEISS Supra 55 VP) at 10 kV was used to study the morphology of the AAO membrane before copper coating, after copper coating, and its cross-section after Ag dendrite formation. The crystalline structure was characterized by X-ray powder diffraction with a Cu K_a source (Siemens D500) scanning from 20° to 90° at the rate of 2° per minute. Metallic elemental analysis was identified using energy-dispersive X-ray spectroscopy (EDX). The single crystal structure analysis was characterized by high resolution transmission electron microscopy (HRTEM, Hitachi H-9500 High-resolution).

Scanning electron microscopy and X-ray diffraction

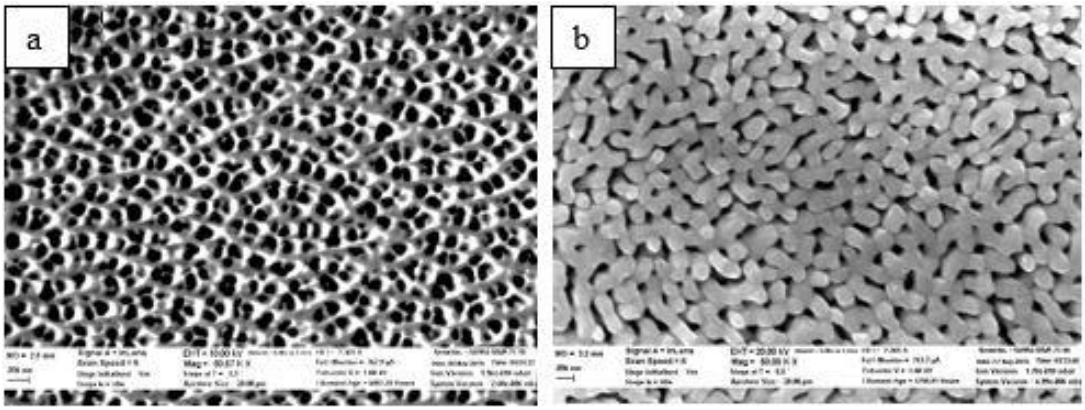

10 a. Bottom part of AAO membrane before Cu coating; b. after Cu coating

The SEM micrographs of the AAO membrane surface before and after copper coating are shown in figure 10 (a) and (b), respectively. Porous structure of AAO membrane was responsible for non-uniform film formation at the bottom. However, coating at the bottom of AAO membrane was continuous.

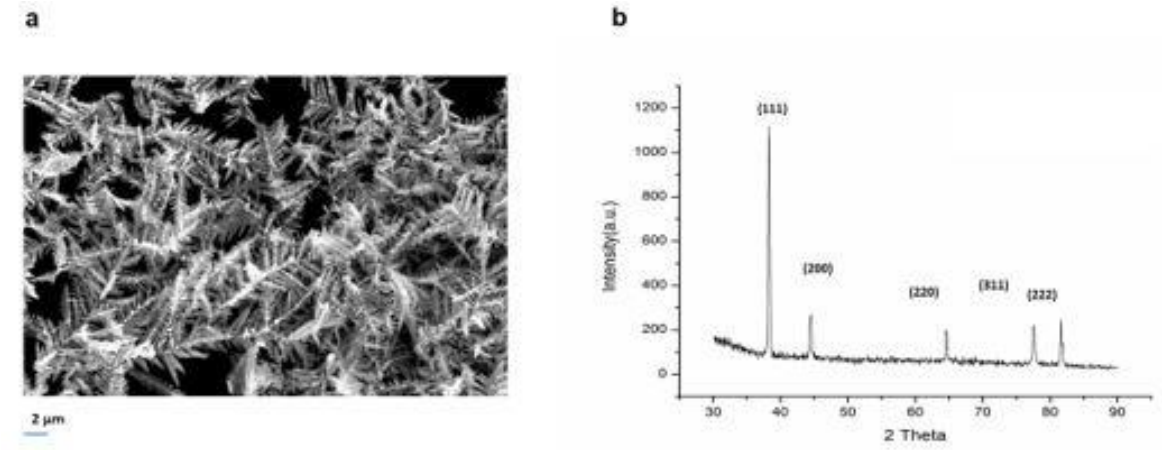

11 a) Low magnification SEM image of the Ag dendrites synthesized with 0.06 M AgNO3 for 180 s. (b) XRD pattern

The SEM image of the Ag dendrites formed using 0.06 M $AgNO_3$ in 180 s is presented in figure 11 (a). Highly uniform Ag dendrites were formed on the top of AAO membrane in relatively short time. Figure 11 (b) represents XRD diffraction pattern of the same Ag dendrite sample. The five observed diffraction peaks were indexed as (111), (200), (220), (311) and (222) which all belong to the FCC structure of Ag lattice. The sharp diffraction peaks indicate that the symmetric Ag dendrites were highly crystalline. It can also be seen that the intensity of (111) peak is very sharp and relatively stronger than other peaks, which could arise from the preferential crystal growth of Ag dendrites along the [111] direction**.** XRD diffraction pattern shows the presence of no elements other than Ag, confirming that the obtained Ag dendrites are pure and single phase.

Morphology of Ag dendrites:

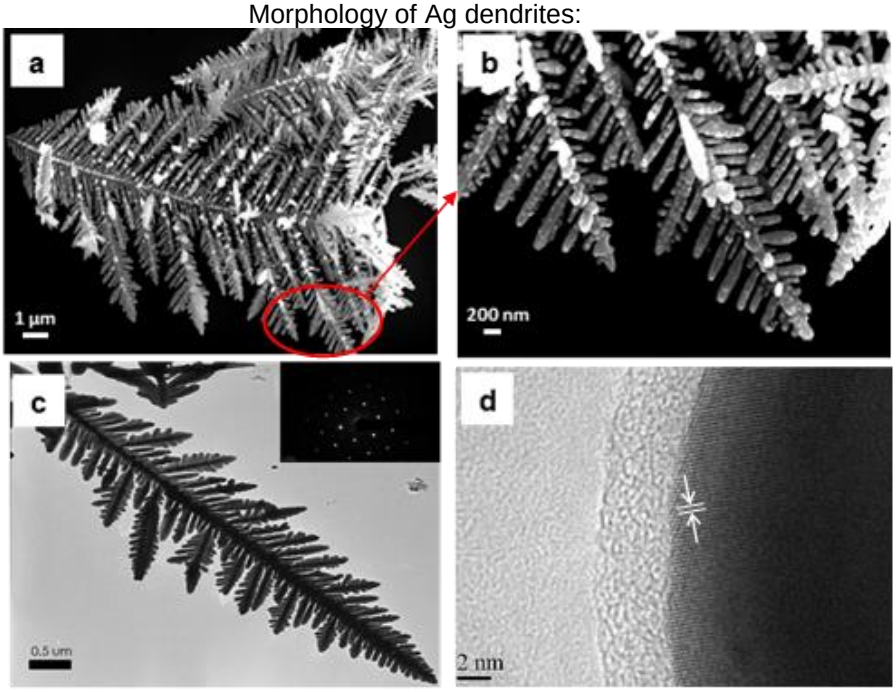

12 (a) SEM image of a typical Ag dendrite obtained at the ions concentrations of 0.06 M after 180 s, (b) high-magnification SEM image from the branches of the Ag dendrite shown in (a), (c) low-magnification TEM image of a typical Ag dendrite with the cores,

The typical morphology of an Ag dendrite produced by 0.06 M $AgNO_3$ solution at 180 s reaction time is presented in figure 12 (a). It is obvious that the Ag dendrite has a 3D multi-level structure composed of a main trunk decorated with several secondary and tertiary branches. A higher magnification SEM image of the branches (shown in figure 12 (b)) exhibits their rough surface possessing several nanometer-sized bumps. A TEM image of the Ag dendrite is shown in figure 12 (c) at a low magnification. The hierarchical structure of the Ag dendrite appears roughly symmetric, where the angles between the trunk and branches are about 55 degree, and the overall length of the Ag dendrite and its branches are about 5 µm and 40 nm, respectively. The corresponding selected area diffraction pattern shown in the inset in figure 12 (c) indicates that the Ag dendrite is single crystal.

The HRTEM image (figure 12 (d)) from the tip of a branch was used to measure the lattice spacing of the edge planes. The distance between the planes was found to be 2.34 Å matching to (111) planes in the Ag crystal (2.35 Å). This suggests that the preferential crystal growth of the branches was along the [111] crystallographic direction, which is consistent with the XRD results.

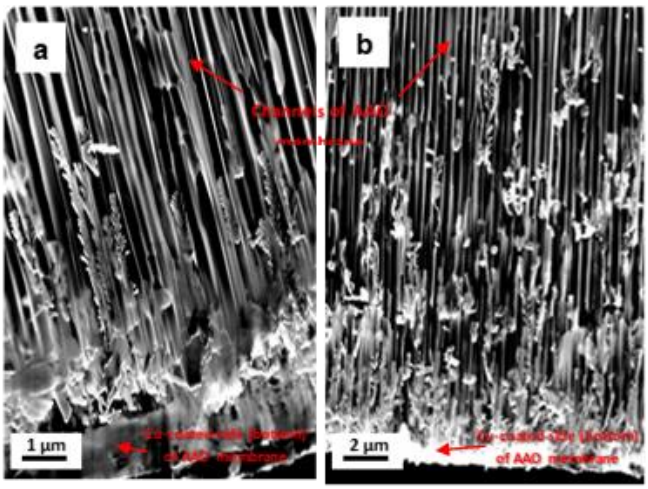

13 SEM image from the cross-section view of the AAO membrane after synthesis Ag dendrites using 0.06 M AgNO3 for reaction time of (a) 120 s, and (b) 11 hours.

Galvanic replacement reaction normally operates through direct redox reaction between the sacrificial and the deposited metals. We can expect that channels inside AAO would be filled with Ag nanostructures to connect Cu at the bottom and Ag dendrites on the top of the membrane. However, from SEM micrographs of the cross-sections of the AAO membrane, it is obvious that there exists no contact between the Cu layer (sacrificial material) and the produced Ag dendrites (deposited metal) on the top surface of the AAO membrane. Thus, the question is that how the Ag dendrites can form far away from Cu surface.

3.4 Proposed Galvanic Replacement Reaction Mechanism

It is obvious that metal Ag is not the result of reducing Ag^+ by Cu, which requires the direct contact of Ag with Cu. There must be other ion(s) involved in this reduction reaction. All possible ions inside solution include: Ag^+, NO_3^-, NO_2^-, Cu^+ and Cu^{2+} First to consider is contribution of NO_3^- in reaction for reduction of Ag^+. Initially it was suspected that the nitrate ions NO_3^- would get reduced by Cu to nitrite ions NO_2^- at the bottom of the AAO membrane and NO_2^- serve as the reducing agent which subsequently reduce Ag^+ ions at the top of the AAO membrane through the following reaction:

$$\mathbf{NO_3^-{}_{(aq)} + 2Cu_{(s)} \rightarrow Cu^{2+} + NO_2^-}\ \textbf{(reaction (I))}$$

It has also been reported that Cu can catalyze the reaction whereby the nitrate ions would convert to nitrite ions. We expected that produced nitrite ions only play the role of intermediate components as they would react with Ag ions and reduce them as follows:

$$\mathbf{Ag^+{}_{(aq)} + NO_2^-{}_{(aq)} \rightarrow Ag_{(s)} + NO_3^-{}_{(aq)}}\ \textbf{(reaction (II))}$$

Experiment was carried out to validate this claim in which we tried to create Ag dendrites in $NaNO_2$ of 1 M concentration solution reacting with 1 M concentration of $AgNO_3$. However, in this experiment we had precipitation of $AgNO_2$ instead of Ag dendrites. This was direct contradiction to our assumption that NO_2^- were responsible for reduction of Ag^+.

Now only possible ion present in the solution which can reduce Ag^+ should be Cu^+. As Cu partially oxidizes to Cu^+ (oxidation reaction); we get counter reaction as reduction of NO_3^- nitrate ions to NO_2^- nitrite ions as mentioned below. Cu^+ can exist in ionic solution and

it travels to the top of AAO membrane through nanochannels where it can interact with abundance volume of Ag^+ and reduce it to Ag.

Partial Oxidation: $2\,Cu \rightarrow 2\,Cu^+ + 2\,e^-$

Reduction reaction: $NO_3^- + 2\,e^- + 2\,H^+ \rightarrow NO_2^- + H_2O$

Overall reaction: $2\,Cu + NO_3^- + 2\,H^+ \rightarrow 2\,Cu^+ + NO_2^- + H_2O$

Ag reduction reaction: $Cu^+ + Ag^+ \rightarrow Ag + Cu^{2+}$

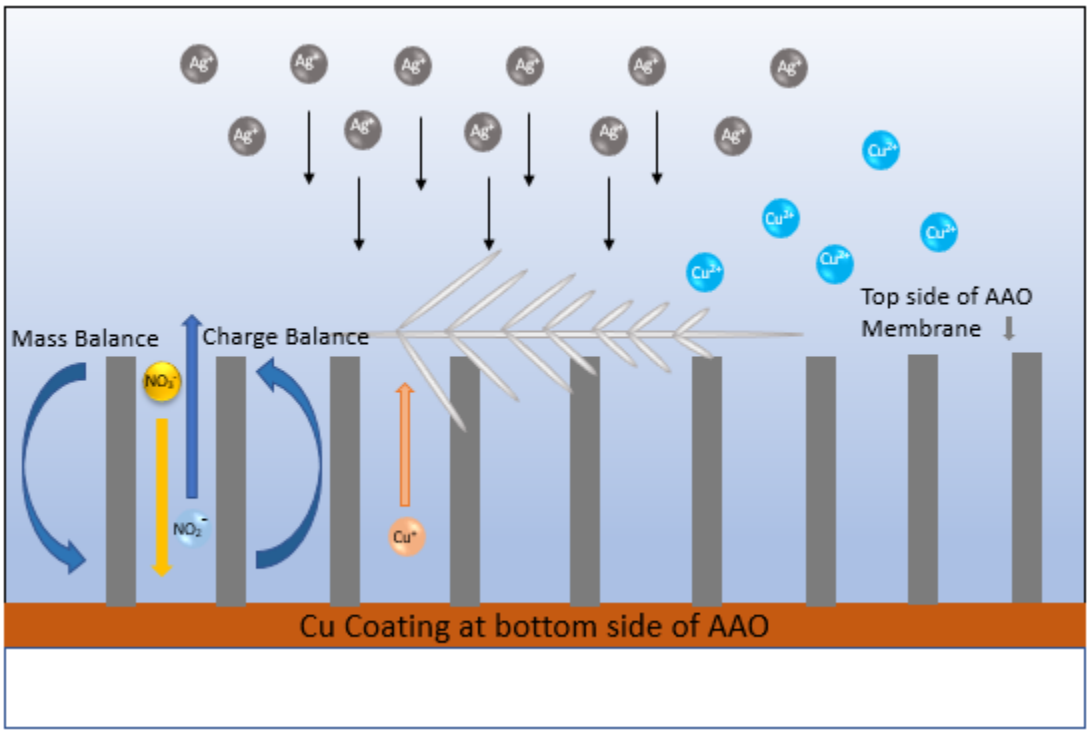

14 Schematic illustration of reaction mechanism

Figure 14 shows the schematic illustration of the proposed mechanism by which Ag dendrites form using AAO membrane. First, as depicted, the $AgNO_3$ solution go down toward the Cu layer through the nanochannels of the AAO membrane. The Ag^+ were reduced directly by the copper atoms through the galvanic replacement reaction ($Cu + 2Ag^+ \rightarrow Cu^{2+} + 2Ag$). Since dendrite growth is a preferential growth mode for Ag atoms

with a very high growth rate, Ag dendrites form at the bottom of the AAO membrane. SEM image from the cross-section of the AAO membrane close to the Cu-coated side after adding 0.06 M $AgNO_3$ solution for 120 s clearly shows the formation of few small Ag dendrites within some of the nanochannels of the AAO membrane. However, due to the limitation of the space inside nanochannels in AAO, a dendrite growth will stop when it reaches to the wall. Meanwhile, with the presence of Ag (Ag acts as catalyst), the NO_3^- ions react with Cu through reaction I and produce NO_2^- and Cu^+. The nanochannels inside AAO membrane limit the dendrite growth, and in turn limit the reduction reaction of Ag^+. This prevention of dendrite growth inside the channels allows Cu^+ reach to the top surface of AAO membrane without reacting with Ag^+.

On the other hand, most of the Ag^+ coming down, due to the concentration gradient, would be consumed by the growing Ag dendrites on the top surface of the AAO membrane before they can reach to the nanochannels. Another cross-section view of the AAO membrane after synthesis of Ag dendrites using 5 ml of 0.06 M $AgNO_3$ for 11 hours is presented in figure 13(b). It is clear that increasing the reaction time for more than 300 times in comparison to the sample shown in figure 13(a) did not change considerably the size and number of Ag dendrites inside the nanochannels of the AAO membrane. This confirms that the interior Ag dendrites were formed by the instantaneous initial nucleation and growth which later were inhibited by the stop of dendrite growth inside the channels.

We conducted a series of tests to determine the presence of nitrite in solution after the reaction using Griess test which is a standard analytical chemistry test. The presence of nitrite ion in solution can be detected by carrying out the greiss reagent test. It is an analytical chemistry test in which color change occurs in case of presence of nitrite ions. It is widely used for the determination of nitrite in potable water. This test is also used for detection of explosives having nitro groups in trace amount [125].

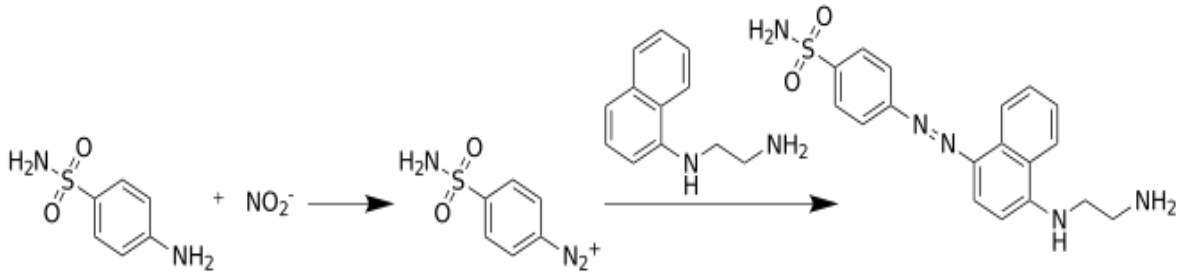

Commercial Griess reagent contains 0.2% naphthylethylenediamine dihydrochloride, and 2% sulphanilamide in 5% phosphoric acid as its typical ingredients.

Detection of nitrites is performed as follows. One drop of the test solution was mixed on a glass plate with one drop of the Griess reagent. Based on the nitrite content in the given solution, a range of colors were formed. from pink (indication: nitrites are moderately present), yellowish (indication: moderate to high concentration of nitrite) to red (indication: intense presence of nitrite), either at once or after standing a short time. Following results were observed.

Table 1: Validation of Greiss Reagent test

	Solutions	Homemade Greiss Reagent	Purchased Greiss Reagent
Time:		15 Minutes	15 Minutes
1	1M $NaNO_2$	Positive (Yellowish)	Positive (Yellowish)
2	1M $NaNO_3$	Negative	Negative
3	1M $CuNO_3$	Negative	Negative
4	1M $AgNO_3$	Negative	Negative

Validity of Greiss reagent test to eliminate the false indication due to other ions was checked by its reaction with 1 M concentration of $NaNO_2$, $NaNO_3$, $CuNO_3$ and $AgNO_3$. Amongst these chemicals only $NaNO_2$ has presence of NO_2^-. Greiss reagent test gave color change only for $NaNO_2$. For $NaNO_3$, $CuNO_3$ and $AgNO_3$ no color change was observed.

Table2: Greiss reagent test for Galvanic replacement reaction

	Solutions	Homemade Greiss Reagent	Purchased Greiss Reagent
Time:		15 Minutes	15 Minutes
1	1M $AgNO_3$ on Cu plate with Filter paper	Positive	Positive
2	1M $AgNO_3$ on Cu plate without Filter paper	Positive	Positive
3	1M $AgNO_3$ on Cu plate with AAO Membrane	Positive	Positive

Greiss reagent test gave positive indication for the presence of NO_2^- when $AgNO_3$ of 1 M concentration was introduce in reaction cell with filter paper and copper plate at the bottom. Similar results were obtained for AAO membrane coated with copper at bottom. These experiments clearly show the presence of NO_2^- in this galvanic reaction.

3.5 Growth Mechanism of Ag Dendrite

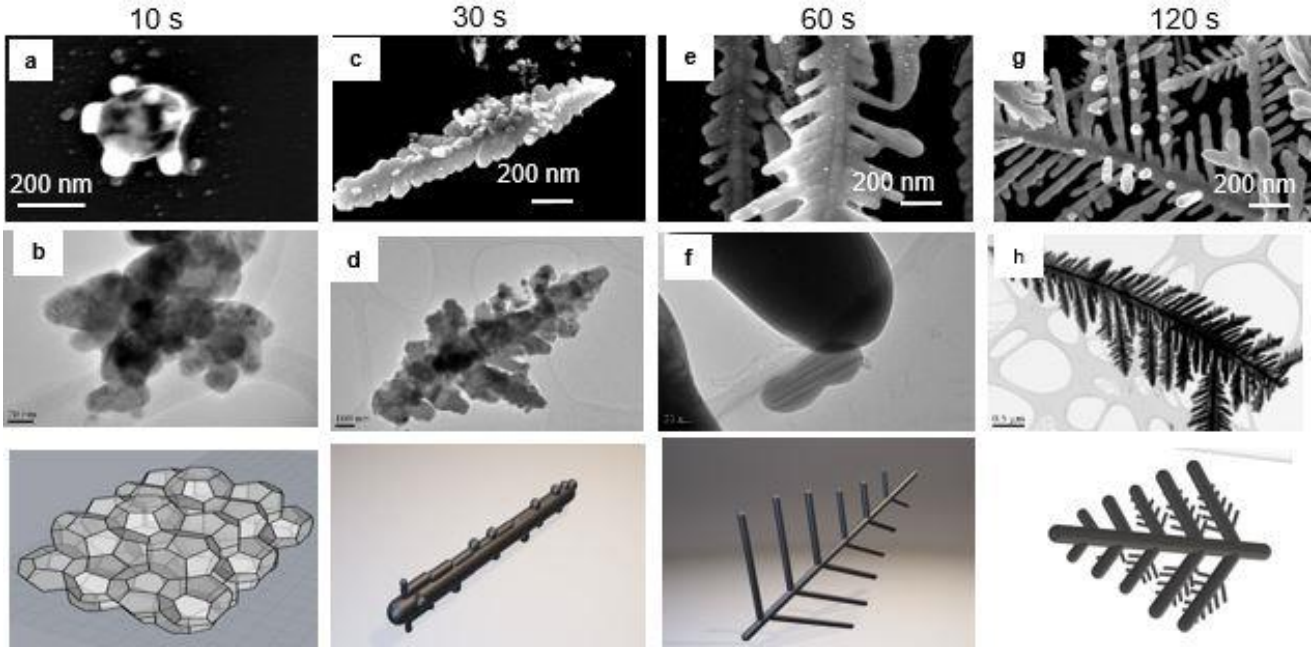

15 Time-dependent study of Ag dendrite growth using 0.06 M AgNO3 solution for reaction time of (a and b) 10 s, (c and d) 30 s, (e and f) 60 s, and (g and h) 120 s (first image of third raw adopted from Designcoding | Weaire-Phelan Structure. (n.d.), from http://www.designcoding.net/weaire-phelan-structure/).

Systematic time-dependent experiments were carried out to get better insight of the growth mechanism of Ag dendrites and their evolution process. These experiments were conducted with a fixed concentration of 0.06 M $AgNO_3$ solution for different reaction times of 10, 30, 60 and 120 seconds. Intermediate products were collected at above

mentioned period to study their morphology and structure. Characterization was done by SEM and TEM, presented in figure 15.

The SEM image of the Ag nanostructure obtained at reaction time interval of 10 s (figure 15 (a)) demonstrates that it consisted of a jagged-shape particle with a core of ~200 nm in diameter and protrusions of ~50 nm. We can see that several small nanoparticles surround this jagged particle. A high magnification TEM image of the same sample (figure 15 (b)) shows that the observed nanostructures are cluster of small irregular Ag nanoparticles that have been partially attached to each other. Many of these nanoparticles are as small as 5 nm.

Increasing the experiment time to 30 s would provide sufficient time for some of the observed nanostructures formed in 10 s to grow and form an imperfect dendrite-like Ag structure of a main trunk with a length around 1 μm, and small, first-generation branches in the range of 100-200 nm (figure 15 (c) and (d)). Here we can still observe Ag nanostructures formed at 10 s of reaction time. The small dendrite-like structures are accompanied with individual and aggregates of nanoparticles. When the reaction proceeded for 60 s (figure 15 (e) and (f)), the branches grow more, creating more resemblance to dendritic structure. As can be seen from the SEM image (figure 15 (e)), the cluster of nanoparticles does not exist anymore after 60 s, whereas the small individual nanoparticles are still present all around and onto the dendrites. Figure 15 (f) depicts a TEM image of one of those nanoparticles (~100 nm) at the tip of a branch.

Increasing the reaction time to 120 s would result in the formation of well-established Ag dendrites with up to four generations of branches closer to the root of the main trunk and one generation of branches at the vicinity of the tip (figure 15 (h)). Another noticeable feature of the sample prepared with 120 s reaction time is the absence of the previously-observed nanoparticles (figure 15 (g)). Instead, a few new branches can be

seen grown upward from the dendrite trunk, which implies to the 3D growth path of the Ag dendrites. All the process over a 120s time interval resulted in the development of 3D, highly-branched Ag dendrites with a main trunk in the micrometer scale and branches from a few nanometers to a few micrometers. Increasing the reaction time from 120 s to 180 s would not alter the morphology and structure of the Ag dendrites, rather enlarges the average size and number of them. The achieved results at different time points can help to better understand the multiple steps occurred during the growth of Ag dendrites through the experimental procedure in this study.

Formation of the anisotropic nanostructure with the intrinsic symmetric cubic crystals in solution is difficult without using any polymer and surfactant agent in a homogeneous solution [126]. It is generally accepted that the non-equilibrium condition in which kinetic factor dominates the thermodynamic one would cause the anisotropic crystal growth for dendritic nanostructures. Several models, including the deposition, diffusion and aggregation (DDA), the diffusion-limited aggregation (DLA), oriented attachment (OA), and the cluster-cluster aggregation (CCA), have been proposed for the formation of Ag dendrites. Amongst these mechanisms, DLA and oriented attachment or a combination of those two have been more popular than other mechanisms to interpret the growth process of Ag dendrites in solution [50, 71].

When the growth rate of metal nanostructure is limited by the diffusion rate of solute atoms to the reaction interface, it is referred as formation of fractal structures through DLA. Whereas in case of oriented attachment, the process of spontaneous self-assembly/alignment of adjacent particles occur so that they share a common crystallographic orientation, which leads to the joining of these particles at a planar interface [127]. In order to understand the growth process of Ag dendrites, consideration of any one of these mechanisms would oversimplify the real phenomena governing growth.

Hence, multiple mechanisms acting simultaneously have been commonly invoked to specify the growth process of Ag dendrites.

At the very beginning, Ag ions are reduced to atoms and come together to form nuclei. Nuclei rapidly grow to form stable nanocrystals. These nanocrystals would have facets which minimizes the total surface energy. Calculations suggest that multiply twinned decahedron with (111) facets would have lowest surface energy. During the nucleation stage, stable multiply twinned decahedron nanoparticles would be abundant in the solution. Through oriented attachment such nanoparticles can stack together to form an elongated structure with (111) facets at the end and with protrusions on the sides. Continuation of the branched aggregates of nanoparticles could continue by diffusion-limited aggregation, oriented attachment, and Ostwald ripening. On further proceeding some of the small nanoparticles diminished by Ostwald ripening. However, some of them might have enough time to relax and fuse to minimum energy positions, thus contributing to the formation of single crystal Ag dendrites.

Better insight to the continuous heterogeneous nucleation and growth of ultra-small Ag nanoparticles during the entire course of the formation of Ag dendrites can be obtained at later stages where some dendrite branches established, as shown in figure 16. It has been proposed that the particle-mediated crystal growth is one of the determining mechanisms of the formation of Ag dendrites inside solutions, in the present experimental procedure, the continuous heterogeneous nucleation and growth has played a major role [72]. This process is thermodynamically favorable as it decreases the overall surface energy of the system. Progress of Ag dendrites into the high Ag^{+} region will result in anisotropic growth of these dendrites. Such dendritic structure will continue to grow and physically adsorb the remaining small nanoparticles once they come in contact to each other. Once the main trunk of fractal nanostructure grow significantly, generation of shorter

branches occur simultaneously, resulting in the formation of well-established, highly-branched dendritic structures.

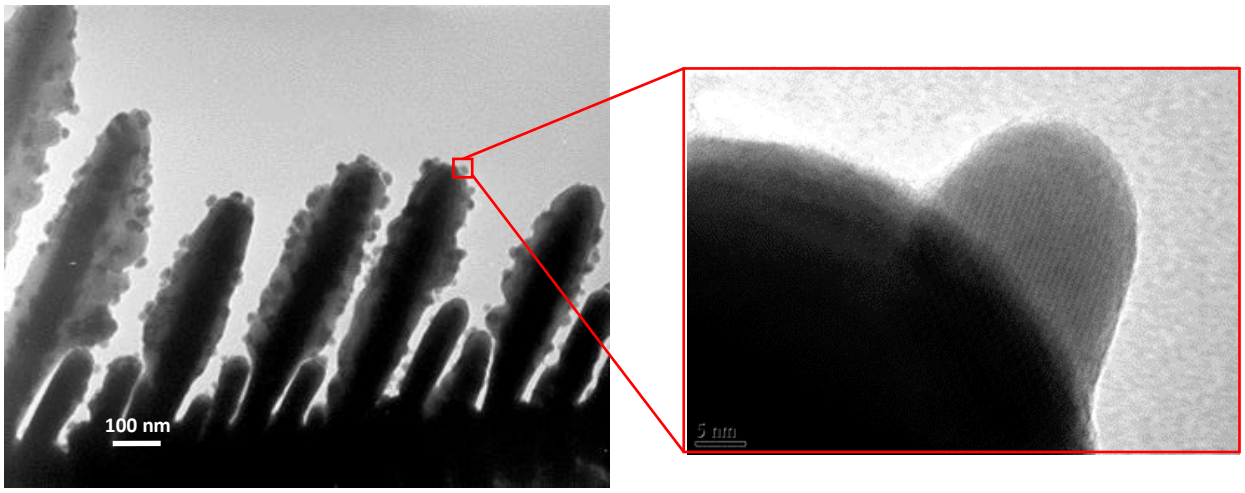

16 TEM images showing the heterogeneous nucleation of Ag nanoparticles on the surface of Ag dendrites.

It should also be noted that another important aspect of the proposed growth mechanism is the hindered growth of the Ag dendrites inside the AAO membrane nanochannels. Such hindered growth of Ag dendrites is attributed because of the spatial constraints, which allow the dendrites grow on the top of AAO membrane.

The TEM image of a complete Ag dendrite synthesized after 180 s using 0.06 M $AgNO_3$ solution along with its corresponding HRTEM images and diffraction patterns are shown in figure 17. The SAD patterns from different locations of the Ag dendrites from its main trunk to the tip of its last branches demonstrates that the dendrite is single crystal. From the top portion of this image it can clearly be observed that the dendrite at the very top was growing through the connection of small Ag nanoparticles, with the preferential growth direction of [112].

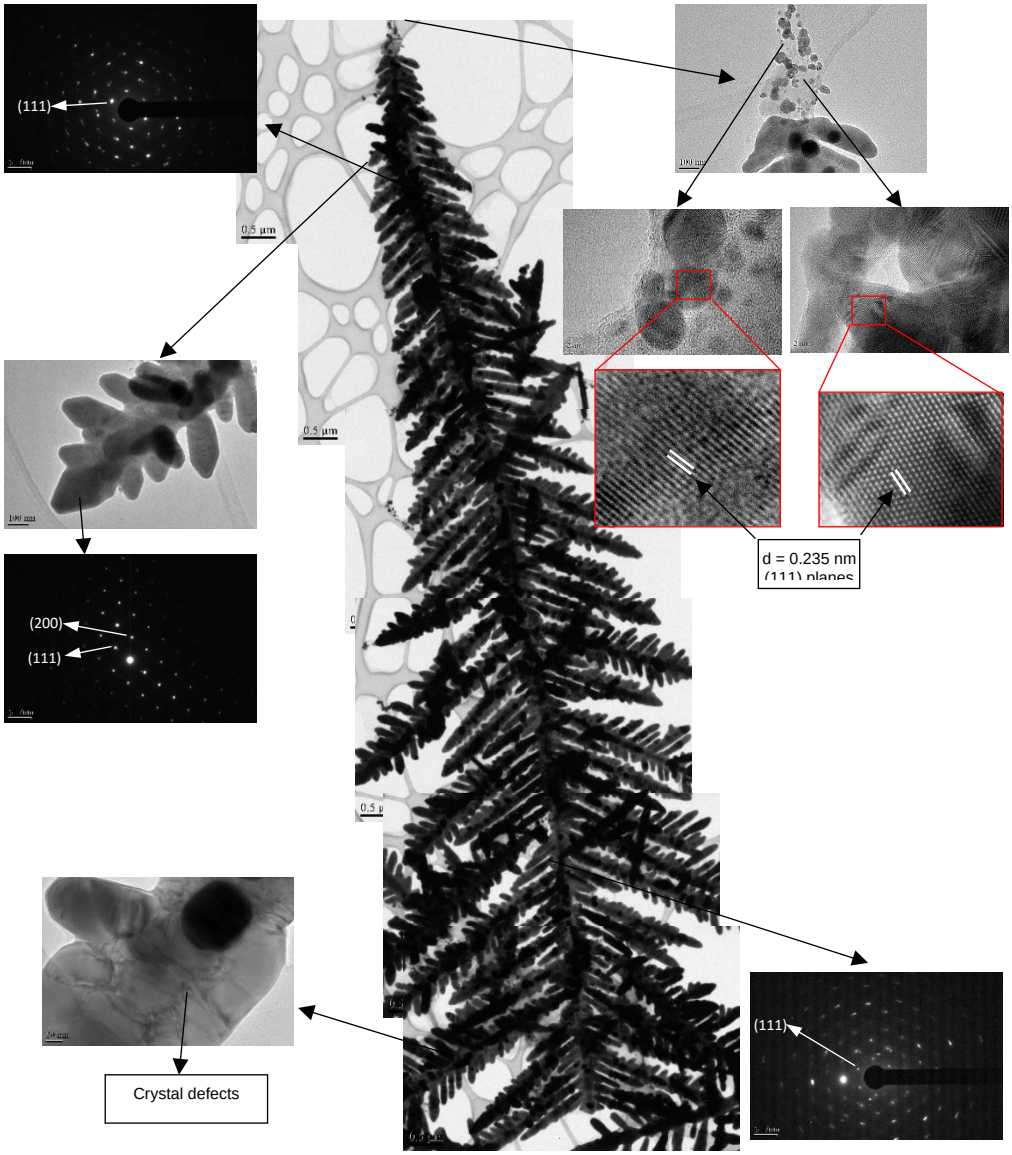

17 TEM image of an Ag dendrite prepared by 0.06 M AgNO3 solution for a reaction time of 180 s.

Certain parameters including concentration gradient, reduction rate, and diffusion, which are all dependent on the initial concentration of the reactants may influence the growth of these Ag dendrites, which starts by formation very small Ag nanoparticles and

grow through a particle-mediated process. It is very important for us to understand the relation between the morphology and structure of the Ag dendrites and reactants concentrations. It can be expected that the product morphology would be strongly determined by the reactant concentrations, as it can affect both the thermodynamic and kinetic characteristics of the reaction.

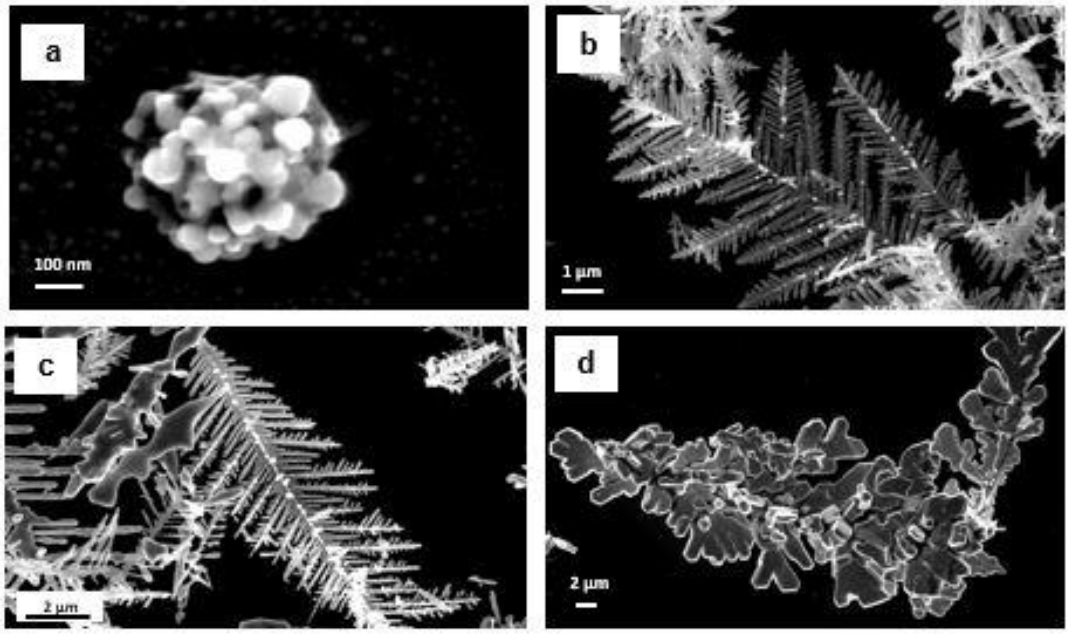

18 SEM images of the Ag dendrites synthesized with various AgNO3 concentrations of (a) 0.01, (b) 0.06, (c) 0.12, and (d) 1 M at a reaction time of 180 s

Above figure 18 represents the SEM images of the Ag structures fabricated at different Ag ion concentrations for a fixed reaction time of 180 s. For $AgNO_3$ solution of M concentration has nanostructure shown in figure 18 (a). Such a low concentration was not sufficient to produce dendritic structure. However, by increasing the concentration of $AgNO_3$ to 0.06 M can produce dendritic nanostructure for 180 s of reaction time. Here it should be noted that lowering the concentration of $AgNO_3$ solution is in fact a decrease in

both the concentration of Ag^+ ions and the amount of reducing agents. Thus, lowering the reactants concentrations from 0.06 M to 0.01 M dramatically changed the obtained Ag products within a reaction time of 180 s. In addition to this, it can be inferred that reducing the concentration had similar effects as lessening the reaction time, without altering the growth mechanism.

Figure 18 (b) and (c) represents Ag dendrites formed at 0.06 and 0.12 M $AgNO_3$ concentrations, respectively. There is no significant change in the morphology of the Ag dendrites by doubling the concentration of $AgNO_3$. However, minor coarsening of the branches can be observed in case of 0.12 M $AgNO_3$ dendrites. Further increase in concentration of $AgNO_3$ to 1 M shows significant change in morphology of dendrites. Although the overall shape of the produced structure still resembles a dendrite, the ordered fine branches were replaced by coarse plate-like stems with polygonal facets at their tips.

Sufficiently high amount of Ag^+ promotes the thermodynamically-favored shapes of multiply-twinned particles (MTPs) [128]. Thus, it is evident that the very high concentration of 1 M caused a significant increase in the reduction rate of Ag ions, enabling the growing Ag structures to become thermodynamically closer to the favorable shapes. Also, it can be considered that higher concentration of Ag^+ ions allowed lateral growth to compete with linear growth as the growth interface is spatially surrounded by a large number of Ag^+ ions without the obligation of a long-order diffusion to compensate their consumption.

3.6 Summary

Systematic study of a new synthesis process for the preparation of highly-branched, single crystal Ag dendrites on the top surface and inside the nanochannels of Cu-coated AAO membranes was carried out. The AAO membranes separated the reactant Cu layer and the product metal Ag, generating completely free-standing, pure, and clean Ag dendrites at the room temperature within a few minutes. Through Greiss reagent test it can be concluded that Ag^+ in $AgNO_3$ solution were not directly reduced by Cu. Instead, Cu partially oxidizes to Cu^+ (oxidation reaction); and counter reaction takes place as reduction of NO_3^- nitrate ions to NO_2^- nitrite ions. Cu^+ can exist in ionic solution and it travels to the top of AAO membrane where it can interact with abundant Ag^+ and reduce it to Ag. This reaction mechanism allows Ag dendrites grow freely on the surface of AAO membrane, while in the interior of the membrane the spatial restrictions retarded the growth of Ag dendrites.

Chapter 4: Three-dimensional Ag Dendritic SERS Substrate

4.1 Introduction

In-situ detection of liquid analyte is highly dependent upon its statistical binding with SERS substrate [129]. Such binding can hugely increase by creating three-dimensional array of Ag dendrites within capillary tube. Two-dimensional SERS substrate cannot provide ease to detect liquid analyte in-situ. Moreover, for certain two-dimensional SERS substrate sample preparation is also required (e.g. evaporation of liquid analyte). To overcome this problem three-dimensional network of Ag dendrites within capillary can serve as a viable solution. Here, three-dimensional array gives aided advantage of large surface area and hence more analyte-substrate interaction. Simple galvanic replacement reaction of $AgNO_3$ with Cu wire was used to create this innovative design of three-dimensional SERS substrate for in-situ detection of liquid media. Experimental procedure to synthesize such a substrate and their SERS activity have been reported in this section.

4.2 Experimental Section

Chemicals and materials:

$AgNO_3$ was purchased from Alfa Aesar (Ward Hill, MA, USA). Square geometry capillary tube with diameter ranging from 200-1000 µm made up with borosilicate glass were purchased from Vitrocom. Latex free syringe of 3 ml from BD medical and copper bus bar wire of 80 µm was purchased from MSC industrial supply Co. They were used as received. Water used throughout all these experiments was purified with a Millipore system.

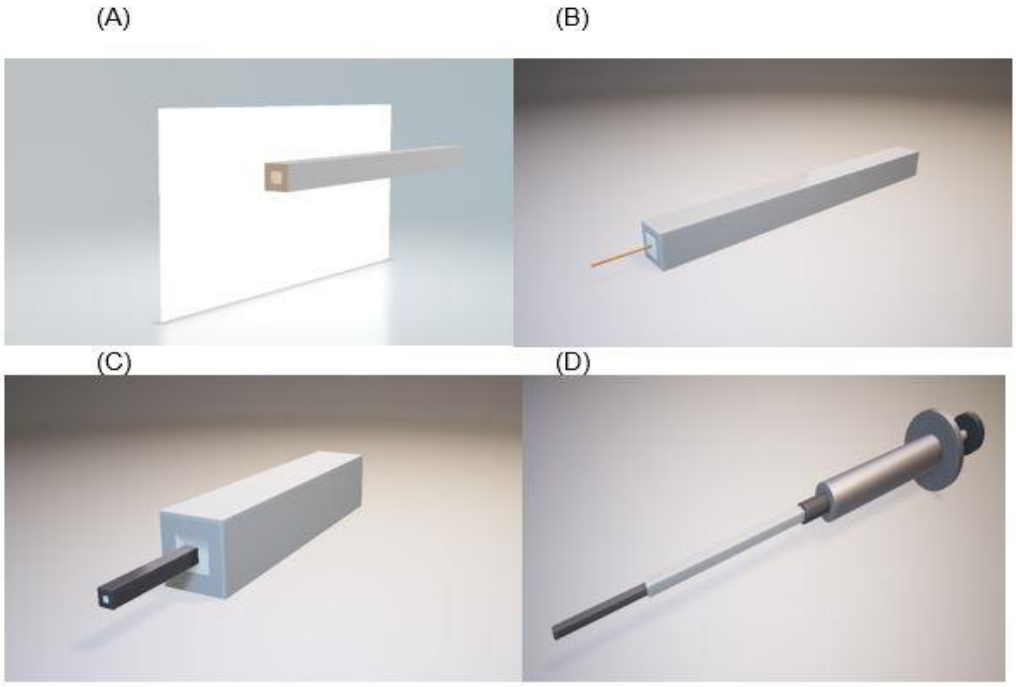

19 Synthesis steps for Ag dendrite formation within capillary

The schematic representation of steps involved to synthesize Ag dendrites on copper bus bar wire within square geometry capillary tube is shown in figure. As shown in figure 19 (A) square geometry capillary tube of borosilicate glass with 500, 700 and 1000 µm of inner diameter was used. Copper bus bar wire with 80 µm diameter was precleaned with ethanol and deionized water to get rid of any contaminants. Copper wire was cut 40 mm in length and inserted into the square capillary tube of 700 µm as shown in figure 19 (B).

Once copper wire was inserted, capillary with 300 µm outer diameter was inserted into 700 µm capillary half way to create tapered structure and it was sealed with UV cured epoxy as illustrated in figure 19 (C). Concentric capillary design makes this substrate compatible to hold three-dimensional network of Ag nanostructured dendrites. This concentric capillary with copper wire in it were connected to syringe through rubber

connector. To prevent leakage from this connection, it was sealed with UV cured epoxy. Figure 19 (D) represents complete experimental setup to synthesize Ag dendritic nano-structures within thin square geometry capillary tube.

$AgNO_3$ solution at different concentrations (0.3, 0.5 and 1 M) were prepared with deionized water. $AgNO_3$ solution was passed through capillary setup for different reaction times (5-10 min, the reaction was stopped by pouring out the $AgNO_3$ solution). Flow rate of AgNO3 solution was kept as low as 0.1 ml/min. Special care was taken while taking pouring out AgNO3 solution to maintain integrity of freshly formed Ag dendritic nanostructures. Prepared substrate was washed with deionized (DI) water for several minutes and air dried for its further application in SERS detection.

4.3 Reaction Mechanism of Ag Dendrite Formation on Copper Wire

Ag dendrites were formed on sacrificial copper wire via simple galvanic replacement reaction (GRR). Galvanic replacement reaction is thermodynamically driven by a favorable difference between reduction potentials of the deposited metal (Ag) and the sacrificial material (Cu bus bar wire). Galvanic replacement method is very effective way to make metallic nanostructures due to its ability to tune the size and shape as well as to change the composition, morphology of the resultant nanostructures. The synthesis parameters comprise of ion concentrations, temperature, and the initial state of the sacrificial material.

The formation of Ag dendrites can be explained by a simple reaction mechanism as follows.

Oxidation reaction: $\mathbf{Cu_{(s)} \rightarrow Cu^{2+} + 2e^-}$

Reduction reaction: $\mathbf{2\ Ag^+ + 2e^- \rightarrow 2Ag}$

The electron comes from the oxidation reaction, $Cu \rightarrow Cu^{2+} + 2e^-$, which takes place at Cu surface where Cu^{2+} is released into the solution, and Ag^+ get reduced to Ag on copper surface by accepting electrons donated by Cu^{2+}. The reduction reaction rate is higher on Ag (111) surface, leading to preferred growth along [111] direction which results in the formation of Ag dendrites.

Overall reaction: $\mathbf{Cu + 2AgNO_3 \rightarrow Cu^{2+} + 2NO_3^- + 2\ Ag}$

Ag ions are reduced to atoms and come together to form nuclei as it was mentioned in previous section. Nuclei rapidly grow to form stable nanocrystals. These

nanocrystals would have facets which minimizes the total surface energy. It has been calculated that multiply twinned decahedron with (111) facets would have lowest surface energy. During the nucleation stage, stable multiply twinned decahedron nanoparticles would be abundant in the solution. These nanoparticles can stack together by oriented attachment to form an elongated structure with (111) facets at the end and with protrusions on the sides, generating a dendrite embryo.

The subsequent growth of the branched aggregates of nanoparticles (dendrite embryo) could continue by several mechanisms, including diffusion-limited aggregation, oriented attachment, and Ostwald ripening. Accordingly, as the reaction proceeds, some of the small nanoparticles diminish by Ostwald ripening, and some of them might have sufficient time to relax and fuse to minimum energy positions, thus contributing to the formation of single crystal Ag dendrites.

(Note- Systematic experiments were carried out to optimize uniformity and reproducible synthesis of Ag dendritic nanostructured three-dimensional substrate. SERS substrate prepared within 700 µm inner diameter capillary tube for 10 mins of reaction time showed uniform distribution of Ag dendrites on copper bus bar wire. Substrates prepared with 3-5 min of reaction time were fragile and couldn't contained by square capillary tube. Hence it was decided to carry out further experiments with 10 mins of reaction time.)

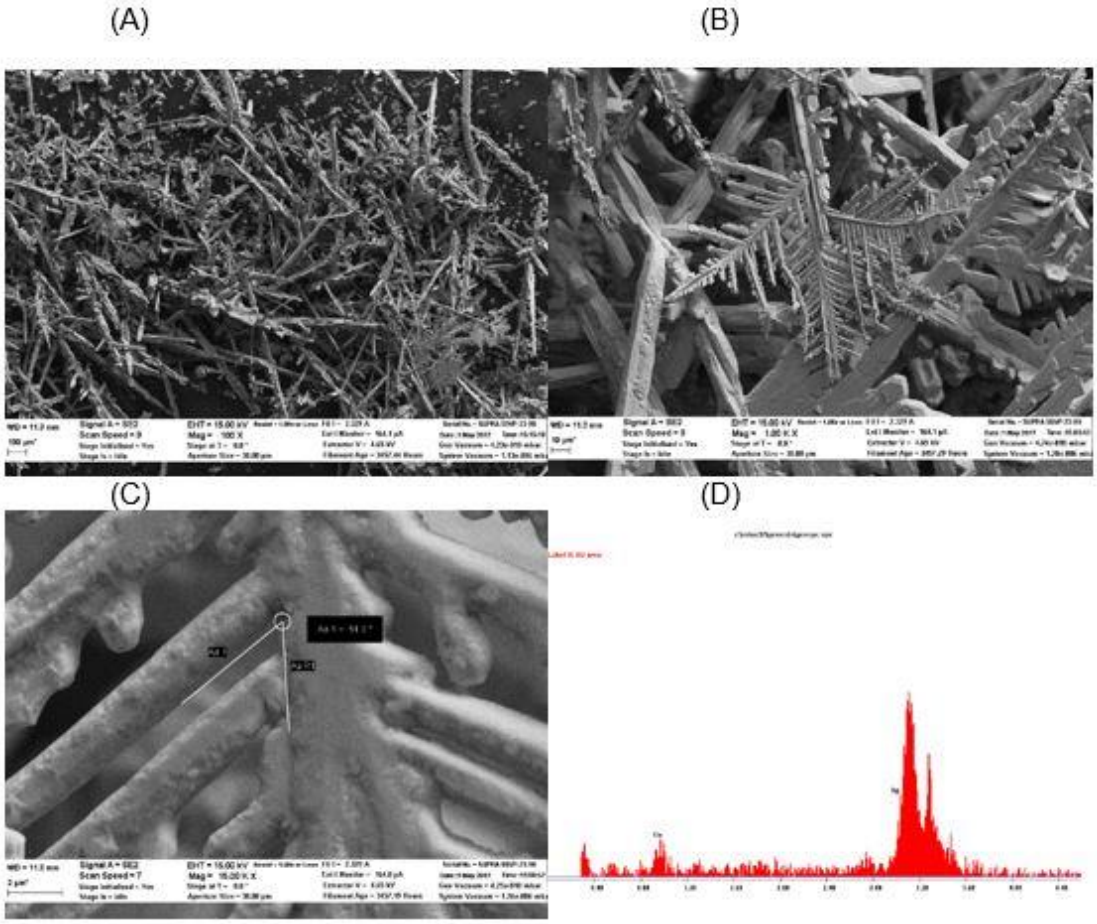

20 SEM and EDS analysis of Ag dendrites prepared with 1 M AgNO3 solution and 10 min of reaction time

Ag dendritic nano-structures prepared with 1 M $AgNO_3$ solution at 10 min of reaction time are presented in figure 20. Figure 20 (D) represents EDS analysis of the same sample. SEM images shown in figure 20 (A), (B) and (C) were obtained with lower, medium, and high magnification respectively. Figure 20 (A) was obtained at 100 X magnification and it is apparent from this image that large amount of rod like structures were formed at 10 min of reaction time. Even though large amount of rod like structures were observed, considerable number of symmetric dendritic structure was present.

Presence of high concentration of Ag^+ and long reaction time lead to formation of rod like structures. Figure 20 (B) at 1.00 KX magnification shows symmetric dendritic structures branched from rod like structure. Average length of main trunk of dendrite is ~70 µm and length of first generation branch ranging from ~5 to ~40 µm. Long range rod like structures have ~10 µm of sides and more than 1000 µm of length. With closer look at figure 20 (B), we can observe that coarse dendritic branches started to merge to form thermodynamically stable structures.

Higher magnification image at 15.00 KX is shown in figure 20 (C). Thick dendritic structure was obtained because of higher concentration of $AgNO_3$ (1 M) and longer reaction time (10 min). Diameter of main trunk is ~4 µm and stems of ~2 µm can be observed from the image. Angular measurement between main trunk and first generation branch is 54.3 degrees which is close to calculated angle between (111) and (200) planes (54.7 degrees). Despite of having coarse dendritic structure it can be expected to have large presence of nanofeatures and nanogaps in the range of 5-100 nm as tip of rod like structures and thick dendrites can form large number of electromagnetic coupling spots. Hence the substrate prepared with 1 M $AgNO_3$ concentration and 10 min reaction time can show good SERS activity. Figure 20 (D) represents EDS results of same sample and it shows significant signal coming from Ag and very weak signal from copper. EDS results gives indirect indication to high yield to the galvanic replacement reaction.

(A) (B)

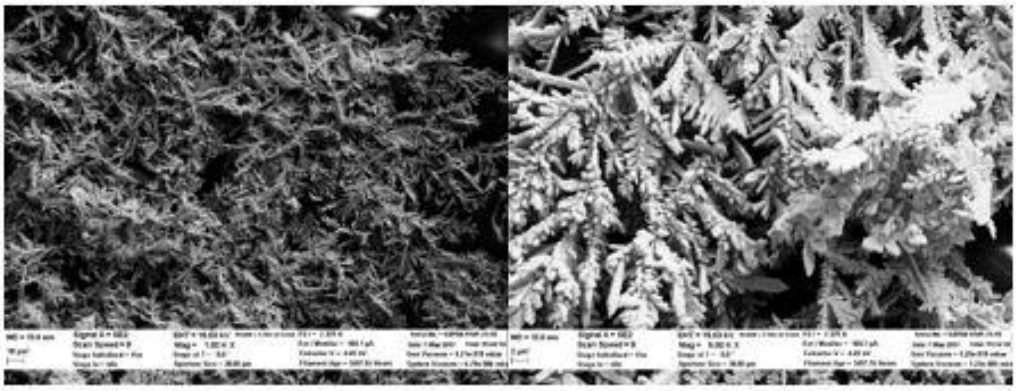

(C) (D)

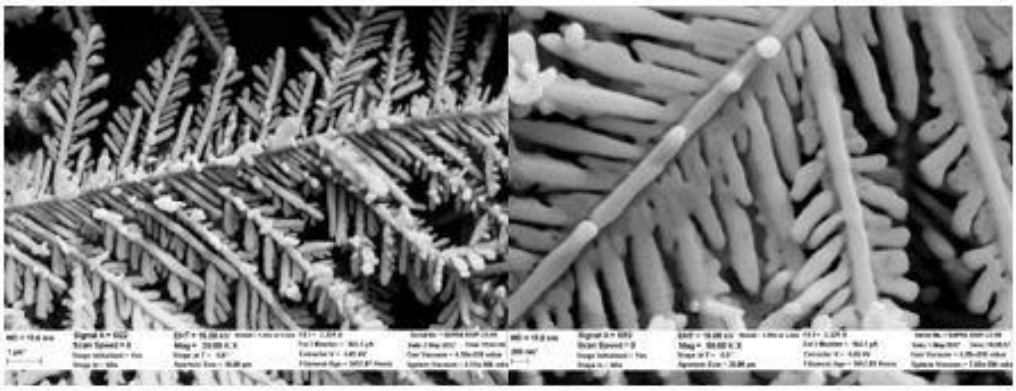

21 SEM analysis of Ag dendrites prepared with 0.5M AgNO3 solution and 10 min of reaction time

Above figure 21 represents SEM micrographs of Ag dendritic nanostructures synthesized with 0.5 M $AgNO_3$ concentration and 10 min of reaction time. Effect of concentration can be studied to get optimum Ag dendritic nanostructure. Figure (A) was taken at 1 KX magnification. It can be seen from figure (A) that Ag dendrites formed with above mentioned synthesis parameters have symmetric structure and high uniformity over

this area. Figure (B) revealed that symmetric Ag dendrites form complex network resulting in huge number of hot spots as mentioned in previous section. A large quantity of Ag dendritic structure with multilevel branch generations are finer as compare to Ag dendrites formed with 1 M $AgNO_3$. It should be noted from figure (A) and (B) that previously existed rod like structures are no longer present at low concentration of $AgNO_3$, leaving behind purely dendritic structures.

High magnification image of sample prepared with 0.5 M $AgNO_3$ and 10 min reaction time was taken at 20.00 KX. It can be clearly seen from high magnification image that by lowering concentration to 0.5 M, obtained dendrites have thickness of 250 nm of main trunk which is much lower as compare to dendrites obtained at 1 M concentration of $AgNO_3$. Synthesized dendrites were very fine in structure having fourth generation of branching. Highly branched structures were obtained having ~200 nm thickness and large number of nanofeatures. Three-dimensional network can be observed with large number of potential hot spots for SERS activity. It can be predicted that such Ag dendritic nanostructures synthesized at 10 min reaction time and 0.5 M of $AgNO_3$ concentration should produce excellent plasmonic activity.

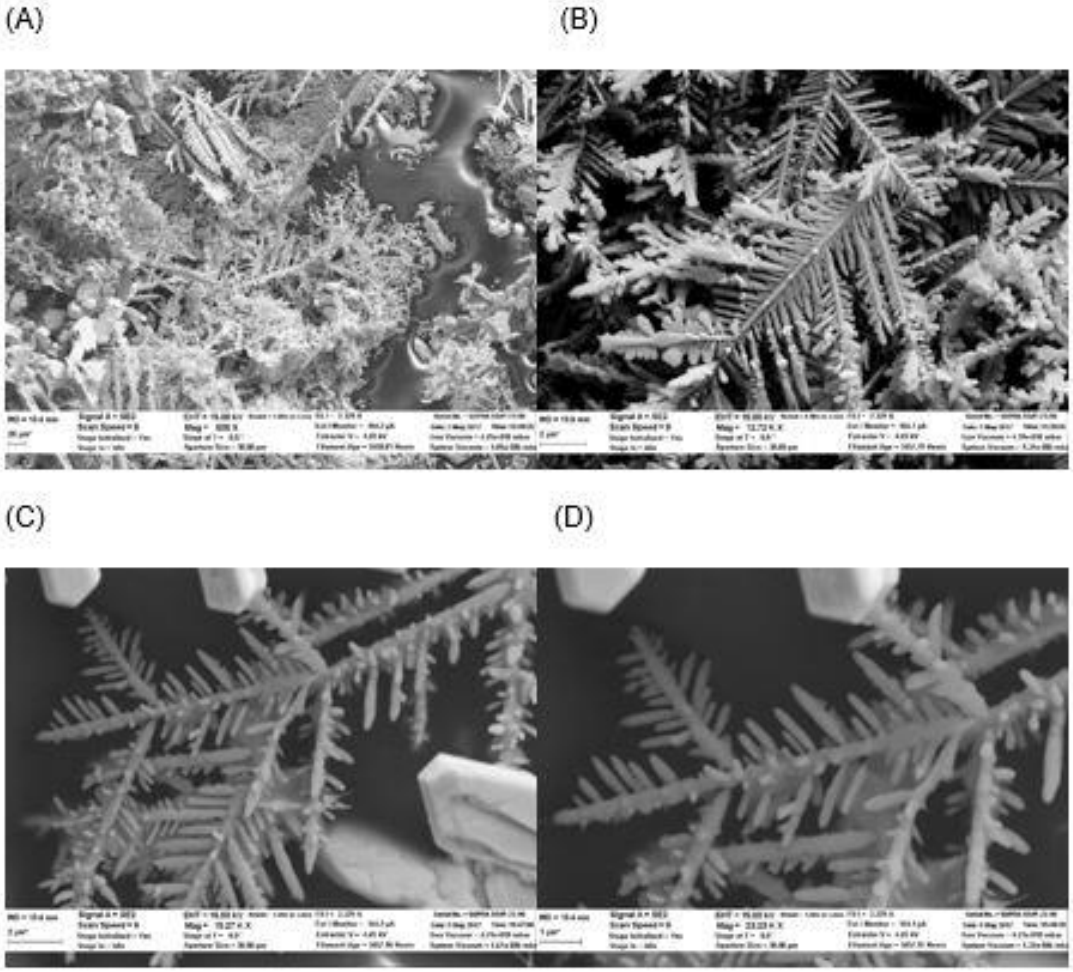

22 SEM images of Ag dendrites taken at low, medium, and high magnifications.

Ag dendrites were obtained by reaction time of 10 min and 0.3 M $AgNO_3$ concentration for SEM analysis. Low magnification SEM image of sample prepared with above mentioned reaction parameters reveals that large number of Ag dendrites were formed. Some of these dendrites were fully grown and were creating long range dendritic network. However, size distribution of dendrites formed at above mentioned reaction

parameters is uneven. Higher magnification images revealed that large number of protrusions are still present on main stem of Ag dendrites. Their dimensions fall in typical rang of 200-250 nm. Presence of large number of protrusions on stems of Ag dendrites are direct indication that dendrites were still growing and were capable to create three-dimensional network.

Series of synthesis experiments and SEM analysis provided information about how concentration as well as reaction time can affect formation of Ag dendritic nanostructures within square capillary tube. Ag dendrites obtained at 0.3 M $AgNO_3$ were non-uniform yielding broad size distribution. Meanwhile Ag dendrites synthesized with 1 M concentration were coarse and showed large number of rod like structures. Despite of having large number of rod like structures, significant hot spots can be observed in terms of interspace between neighboring branches, the tips of stems and tips of rods. However Ag dendrites produced with 0.5 M $AgNO_3$ solution gave most symmetric structure with highly uniform distribution of Ag dendrites. Ag dendrites not only show their spread laterally but also vertically. Interspace between neighboring branches reduces which is in favor of producing sufficient hot spots for excellent SERS activity.

Ag dendrites synthesized with 1 M $AgNO_3$ concentration showed uniform deposition of Ag as compare to 0.5 M $AgNO_3$ for same duration of reaction time. Hence it was decided to carry out further experiments with 1 M $AgNO_3$ concentration to investigates SERS activity and liquid media detection limit.

4.4 Surface-enhanced Raman Scattering (SERS) measurement

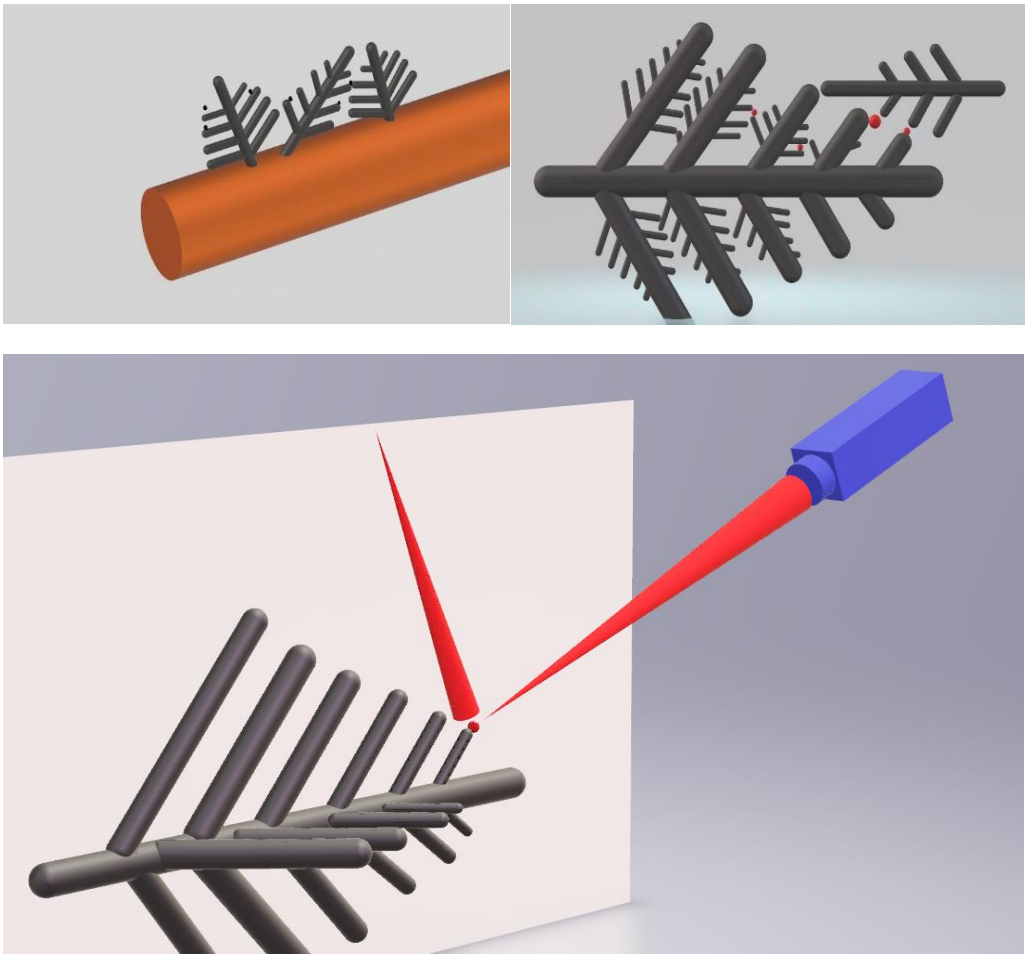

23 Schematic diagram of SERS measurement of substrate

Figure 23 shows the schematic diagram of Ag dendritic nanostructures on copper wire forming three-dimensional substrate. Syringe was used to pump liquid solution of rhodamine 6G (R6G) through capillary. As shown in figure 23 rhodamine 6G molecules adsorbed on Ag dendritic nanostructures and Raman spectra was obtained. Aqueous solution of R6G was prepared with different 10^{-3} to 10^{-11} M and used to investigate SERS

activity of substrate. Stock solution of 10^{-3} M R6G was diluted to make range of solutions up to 10^{-11} M R6G for in-situ liquid media detection. SERS spectra were recorded using Horiba Raman Spectrometer with a 633 nm of excitation laser source and equipped with a diffraction grating of 1200 lines mm^{-}. System was connected to microscope of 50 X objective lens to focus laser source and collect the stokes-shifted Raman signals. Instrument calibration was carried out with the Raman signal from a silicon standard sample at 520 cm^{-} with 30 seconds of integration time. Data obtained is without any baseline correction for fluorescence band.

Spectra of 10^{-3} M R6G solution was obtained without SERS substrate and with SERS substrate. Following results were obtained:

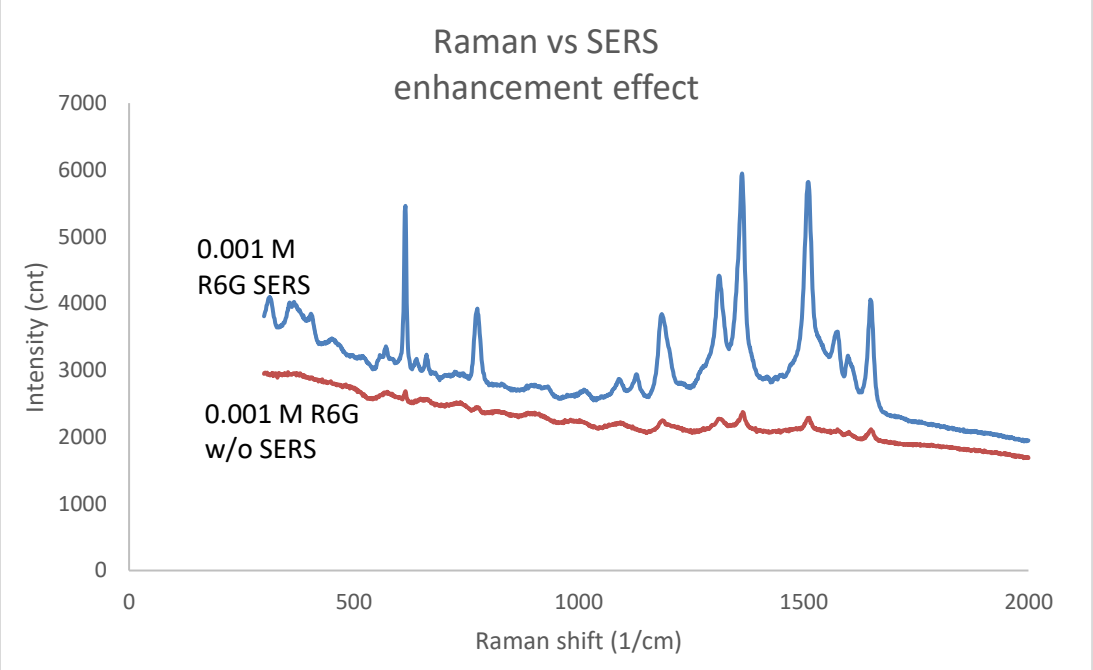

Graph A Enhancement effect of SERS substrate

Graph A represents Raman spectra of 10^{-3} M of R6G in which x-axis is Raman shift (cm^{-1}) and y-axis is intensity (cnt). It is clear from the figure 24 that SERS substrate showed excellent enhancement. Spectra obtained without SERS spectra showed characteristic Raman peaks of R6G: 610, 767, 1184, 1360, 1510, 1570 and 1651 cm^{-1}, which correspond to C-C-C ring in-plane, C-H out of plane bending, C-H in-plane bending vibrations, C-O-C stretching and C-C stretching of ring [130]. It should be noted that peak at 610 cm^{-1} with SERS substrate show intensity enhancement of ~1000 times from baseline as compare to spectra of R6G without SERS substrate in liquid media.

The practical application of Raman scattering analysis is dependent of SERS activity of substrate. To determine detection limit for SERS substrate, aqueous solution of R6G from 10^{-3} M - 10^{-9} M was systematically investigated with 633 nm of laser excitation source and 30 seconds of integration time on Horiba Raman Spectrometer. Following results were obtained:

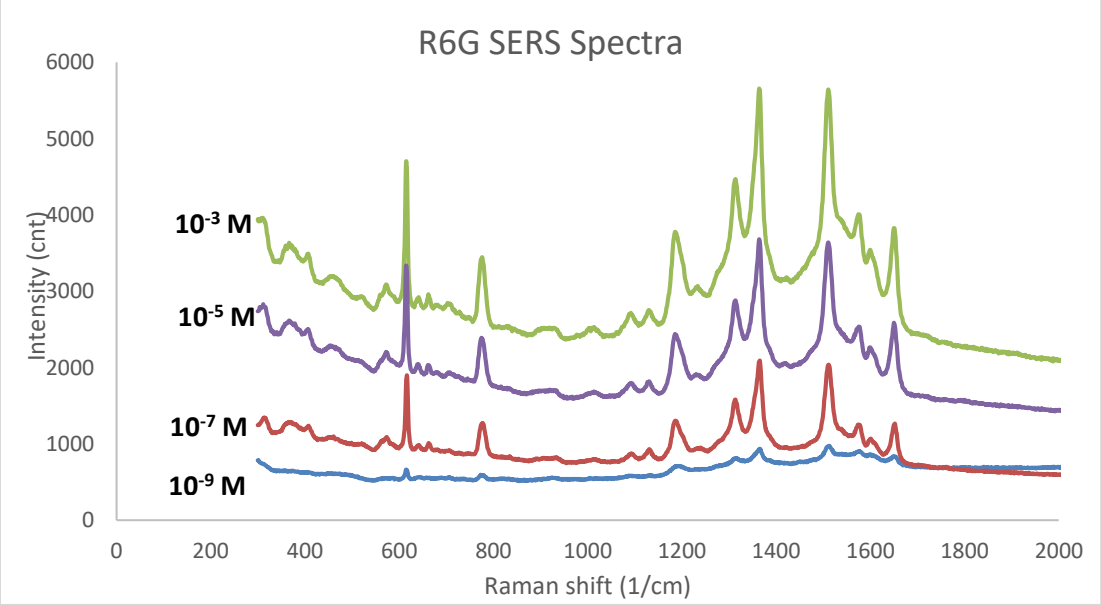

Graph B SERS spectra of R6G at different concentrations (from 10^{-3} to 10^{-9} M) using SERS substrate

SERS measurements were performed over substrate by linear scanning with detection spot size of 50 µm. Systematic measurements of SERS spectra were carried out on SERS substrate prepared with 10 min reaction time and 1 M $AgNO_3$ concentration. SERS spectra of 10^{-9} M R6G was first obtain by putting a drop of solution in capillary. By linear scanning above shown spectra was obtained. Real time display (RTD) showed significant peaks by merely focusing laser on substrate at any random spots. As R6G solution was pumped through Ag dendrite SERS three-dimensional substrate, intensity enhancement was observed for the same concentration of solution.

Once R6G spectra of 10^{-9} M was obtained, SERS substrate was washed with DI water for several minutes (20 min). Similar approach was opted for detection of 10^{-7} M, 10^{-5} M, and 10^{-3} M R6G solution in DI water. We must note here that there is no significant change to intensity enhancement for R6G solution with greater than and equal to 10^{-7} M concentration which is because of saturation of SERS signal intensity. However, SERS intensity for 10^{-9} M R6G drops drastically. Real time display (RTD) showed instant results for these concentrations of R6G and they were acquired subsequently.

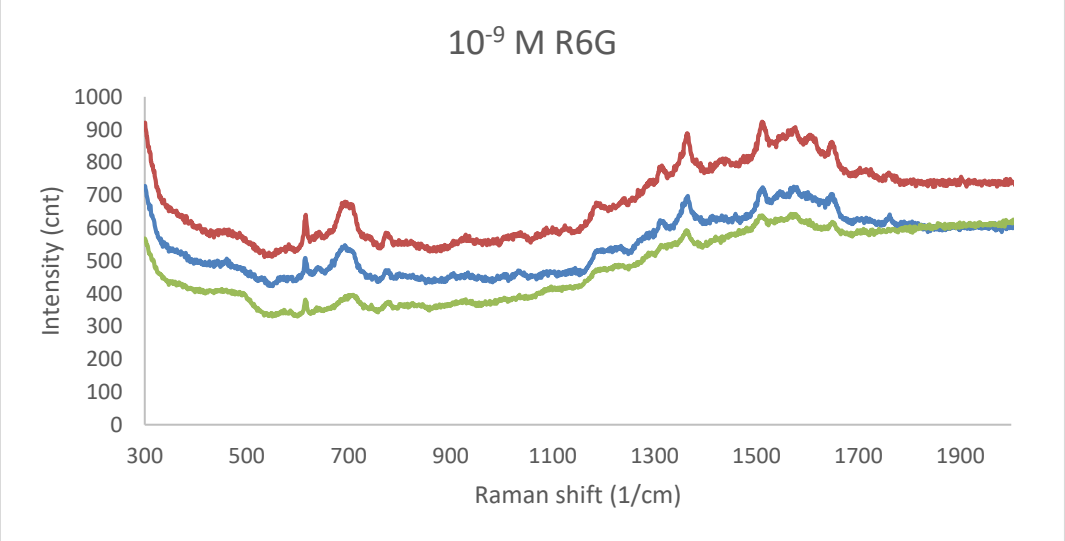

Graph C SERS spectra of R6G at different spots with 10^{-9} M concentration

Raman spectra of R6G at 10^{-9} M concentration was taken at three random spots on substrate. All three random spots showed major peaks on real time display and subsequently their SERS spectra were acquired. Despite of showing major peaks at random spots their intensity varied. Further, to get lower detection limit R6G solution in DI water of 10^{-10} M and 10^{-11} M concentration were checked with SERS substrate. Following results were obtained:

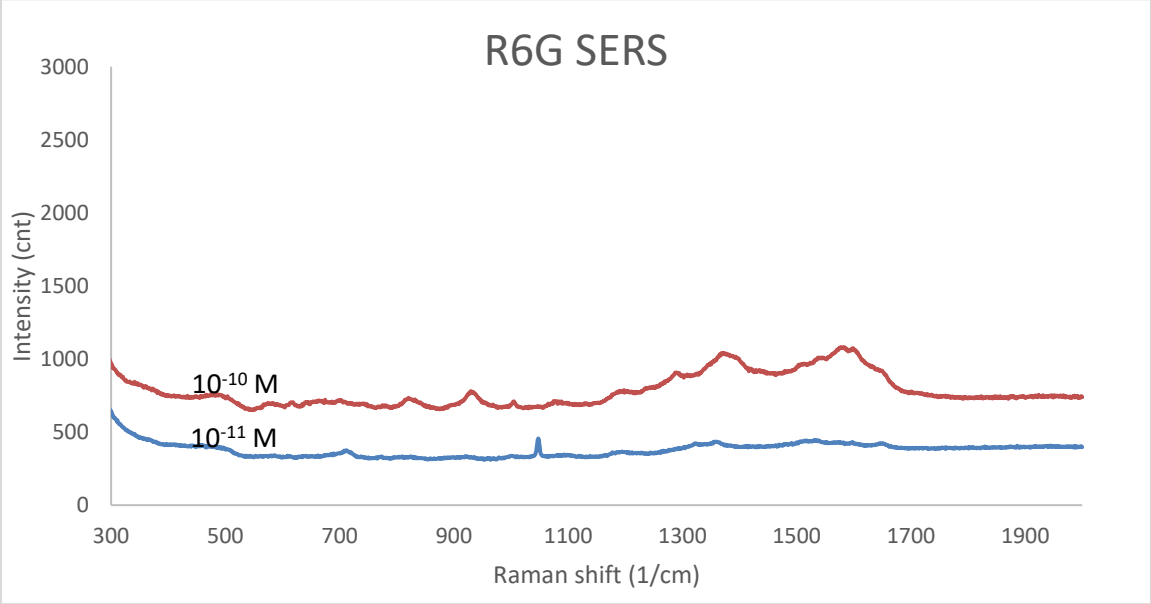

Graph D SERS spectra of R6G at 10^{-10} M and 10^{-11} M concentration

New SERS substrate was prepared with 1 $AgNO_3$ concentration as mentioned in synthesis section to investigate lower detection on analyte concentration. R6G of 10^{-11} M concentration was passed in capillary and checked under Raman spectrometer. In order for us to get SERS result, excitation source with 633 nm wavelength was used and integration time was increased to 40 seconds from previous integration time of 30 seconds. Here intensity of peaks diminished significantly as expected. However, detection of 10^{-11}

M R6G was carried out in similar time as it was taken for higher concentrations. Similarly, SERS spectra for 10^{-10} M R6G concentration was obtained and it is shown in figure.

4.5 Summary

Three-dimensional Ag dendritic SERS substrate made within square geometry capillary tube showed excellent SERS response. Experimental results indicate that synthesis of robust SERS substrate within square capillary can be achieved by keeping high concentration of $AgNO_3$ solution. SERS substrates prepared with 1 M $AgNO_3$ concentration with 10 minutes of reaction time were uniform in distribution of Ag dendrites within square geometry capillary tube. SERS signals were obtained by simply focusing laser beam on SERS substrate at any random spots. We could obtain detection limit of 10^{-11} M of R6G. This SERS substrate has the potential to detect liquid analyte in-situ with very high sensitivity and specificity.

Chapter 5 Conclusion

In summary, a new synthesis process for the preparation of highly-branched, single crystal Ag dendrites on the top surface and inside the nanochannels of Cu-coated AAO membranes was systematically studied. The AAO membranes separated the reactant Cu layer and the product metal Ag, generating completely free-standing, pure, and clean Ag dendrites at the room temperature within a few minutes. It was concluded that Ag^+ in $AgNO_3$ solution were not directly reduced by Cu. Rather, Cu partially oxidizes to Cu^+ (oxidation reaction); and counter reaction takes place as reduction of NO_3^- to NO_2^-. Cu^+ can exist in ionic solution and it travels to the top of AAO membrane where it can interact with abundance volume of Ag^+ and reduce it to Ag. This reaction mechanism allows Ag dendrites grow freely on the surface of AAO membrane, while in the interior of the membrane the growth of the Ag dendrites was retarded by the spatial restrictions.

Series of time-dependent experiments revealed that the synthesis of Ag dendrites starts with formation of very small nanoparticles which subsequently bind together to create nanocluster. The growth of the nanocluster proceeds by diffusion limited aggregation (DLA), oriented attachment, and Oswald ripening. It was found that increasing the concentration of $AgNO_3$ solution to 1M can enforce the Ag products to take thermodynamically stable shapes. However, it has also been found that galvanic replacement reaction highly dependent upon the available volume of $AgNO_3$ solution. In case of galvanic replacement reaction in thin walled square geometry capillary tubes, 1M $AgNO_3$ solution can be used to form symmetric dendrite structure.

An innovative design of Ag dendritic nanostructures within square geometry capillary tube was developed. Simple galvanic replacement reaction route was used to prepare this substrate. Novel design of Ag dendritic nanostructured SERS substrate provides uniform distribution of electromagnetic coupled hotspots. SERS substrate has

complex network of dendrites and it has a large area to adsorb analyte molecules on its surface. Structure of such SERS substrate was optimized by controlling concentration of $AgNO_3$ solution and reaction time of galvanic replacement reaction. 1M $AgNO_3$ solution concentration and 10 minutes of reaction time was proved to be an optimum condition to form uniform distribution of Ag dendrite yielding robust SERS substrate. The synthesized substrate exhibit excellent SERS performance with high sensitivity, good reproducibility and better tunability. SERS detection limit of 10^{-11} M was achieved for in-situ liquid media detection. Results were reproducible over entire area of substrate and hence this substrate can be an excellent candidate for in-situ liquid media detection for low concentration of analyte.

References

1. S.L. Kleinman, R.R. Frontiera, A.I. Henry, J.A. Dieringer, R.P.V. Duyne Creating, characterizing, and controlling chemistry with SERS hot spots Phys. Chem. Chem. Phys., 15 (2013), pp. 21–36
2. B. Sharma, R.R. Frontiera, A.I. Henry, E. Ringe, R.P.V. Duyne SERS: materials, applications, and the future Mater. Today, 15 (2012), pp. 16–25
3. M. Fan, G.F.S. Andrade, A.G. Brolo A review on the fabrication of substrates for surface enhanced Raman spectroscopy and their applications in analytical chemistry Anal. Chim. Acta, 693 (2011), pp. 7–25
4. Jeanmaire, D. L., & Van Duyne, R. P. (1977). Surface Raman spectroelectrochemistry: Part I. Heterocyclic, aromatic, and aliphatic amines adsorbed on the anodized silver electrode. *Journal of electroanalytical chemistry and interfacial electrochemistry*, *84*(1), 1-20.
5. Kneipp, K., Wang, Y., Kneipp, H., Perelman, L. T., Itzkan, I., Dasari, R. R., & Feld, M. S. (1997). Single molecule detection using surface-enhanced Raman scattering (SERS). *Physical review letters*, *78*(9), 1667.
6. Nie, S., & Emory, S. R. (1997). Probing single molecules and single nanoparticles by surface-enhanced Raman scattering. *science*, *275*(5303), 1102-1106.
7. Wang, H. H., Liu, C. Y., Wu, S. B., Liu, N. W., Peng, C. Y., Chan, T. H., ... & Wang, Y. L. (2006). Highly raman-enhancing substrates based on silver nanoparticle arrays with tunable sub-10 nm gaps. *Advanced Materials*, *18*(4), 491-495.
8. Dieringer, J. A., Lettan, R. B., Scheidt, K. A., & Van Duyne, R. P. (2007). A frequency domain existence proof of single-molecule surface-enhanced Raman spectroscopy. *Journal of the American Chemical Society*, *129*(51), 16249-16256.

9. Grabar, K. C., Freeman, R. G., Hommer, M. B., & Natan, M. J. (1995). Preparation and characterization of Au colloid monolayers. *Analytical chemistry*, *67*(4), 735-743.
10. Rivas, L., Sanchez-Cortes, S., Garcia-Ramos, J. V., & Morcillo, G. (2000). Mixed silver/gold colloids: a study of their formation, morphology, and surface-enhanced Raman activity. *Langmuir*, *16*(25), 9722-9728.
11. Reiner EJ, Clement RE, Okey AB, Marvin CH (2006) Advances in analytical techniques for polychlorinated dibenzo-p-dioxins, polychlorinated dibenzofurans and dioxin-like PCBs. Anal Bioanal Chem 386(4):791–806
12. Pushkarsky, M. B., Dunayevskiy, I. G., Prasanna, M., Tsekoun, A. G., Go, R., & Patel, C. K. N. (2006). High-sensitivity detection of TNT. *Proceedings of the National Academy of Sciences*, *103*(52), 19630-19634.
13. Baker, B. R., Lai, R. Y., Wood, M. S., Doctor, E. H., Heeger, A. J., & Plaxco, K. W. (2006). An electronic, aptamer-based small-molecule sensor for the rapid, label-free detection of cocaine in adulterated samples and biological fluids. *Journal of the American Chemical Society*, *128*(10), 3138-3139.
14. Squires, T. M., Messinger, R. J., & Manalis, S. R. (2008). Making it stick: convection, reaction and diffusion in surface-based biosensors. *Nature biotechnology*, *26*(4), 417.
15. Fang Y, Seong N-H, Dlott DD (2008) Measurement of the distribution of site enhancements in surface-enhanced Raman scattering. Science 321(5887):388–392
16. Michaels AM, Jiang, Brus L (2000) Ag nanocrystal junctions as the site for surface-enhanced Raman scattering of single Rhodamine 6G molecules. J Phys Chem B 104(50):11965–11971
17. Bosnick KA, Jiang, Brus LE (2002) Fluctuations and local symmetry in single-molecule Rhodamine 6G Raman scattering on Ag nanocrystal aggregates. J Phys Chem B 106(33):8096–8099

18. Dieringer JA, Lettan RB 2nd, Scheidt KA, Van Duyne RP (2007) A frequency domain existence proof of single-molecule surface-enhanced Raman spectroscopy.
19. Fang, J., Hahn, H., Krupke, R., Schramm, F., Scherer, T., Ding, B., & Song, X. (2009). Silver nanowires growth via branch fragmentation of electrochemically grown silver dendrites. *Chemical Communications*, (9), 1130-1132.
20. Zhang, J. H., Liu, H. Y., Zhan, P., Wang, Z. L., & Ming, N. B. (2007). Controlling the growth and assembly of silver nanoprisms. *Advanced Functional Materials*, *17*(9), 1558-1566.
21. Liang, H., Li, Z., Wang, W., Wu, Y., & Xu, H. (2009). Highly Surface-roughened "Flower-like" Silver Nanoparticles for Extremely Sensitive Substrates of Surface-enhanced Raman Scattering. *Advanced Materials*, *21*(45), 4614-4618.
22. Zhu, C., Meng, G., Huang, Q., Zhang, Z., Xu, Q., Liu, G., ... & Chu, Z. (2011). Ag nanosheet-assembled micro-hemispheres as effective SERS substrates. *Chemical Communications*, *47*(9), 2709-2711.
23. Cheng, Z. Q., Nan, F., Yang, D. J., Zhong, Y. T., Ma, L., Hao, Z. H., ... & Wang, Q. Q. (2015). Plasmonic nanorod arrays of a two-segment dimer and a coaxial cable with 1 nm gap for large field confinement and enhancement. *Nanoscale*, *7*(4), 1463-1470.
24. Fei Chan, Y., Xing Zhang, C., Long Wu, Z., Mei Zhao, D., Wang, W., Jun Xu, H., & Sun, X. M. (2013). Ag dendritic nanostructures as ultrastable substrates for surface-enhanced Raman scattering. *Applied Physics Letters*, *102*(18), 183118.
25. Gu, C., & Zhang, T. Y. (2008). Electrochemical synthesis of silver polyhedrons and dendritic films with superhydrophobic surfaces. *Langmuir*, *24*(20), 12010-12016.
26. Qin, X., Miao, Z., Fang, Y., Zhang, D., Ma, J., Zhang, L., ... & Shao, X. (2012). Preparation of dendritic nanostructures of silver and their characterization for electroreduction. *Langmuir*, *28*(11), 5218-5226.

27. Mandke, M. V., Han, S. H., & Pathan, H. M. (2012). Growth of silver dendritic nanostructures via electrochemical route. *CrystEngComm*, *14*(1), 86-89.
28. Sivasubramanian, R., & Sangaranarayanan, M. V. (2015). A facile formation of silver dendrites on indium tin oxide surfaces using electrodeposition and amperometric sensing of hydrazine. *Sensors and Actuators B: Chemical*, *213*, 92-101.
29. Sharma, D. K., Ott, A., O'Mullane, A. P., & Bhargava, S. K. (2011). The facile formation of silver dendritic structures in the absence of surfactants and their electrochemical and SERS properties. *Colloids and Surfaces A: Physicochemical and Engineering Aspects*, *386*(1-3), 98-106.
30. Chu, J., Zhao, Y., Li, S. H., Li, W. W., Chen, X. Y., Huang, Y. X., ... & Liu, G. (2015). A highly-ordered and uniform sunflower-like dendritic silver nanocomplex array as reproducible SERS substrate. *Rsc Advances*, *5*(5), 3860-3867.
31. Bian, J., Shu, S., Li, J., Huang, C., Li, Y. Y., & Zhang, R. Q. (2015). Reproducible and recyclable SERS substrates: Flower-like Ag structures with concave surfaces formed by electrodeposition. *Applied Surface Science*, *333*, 126-133.
32. Sawangphruk, M., Sanguansak, Y., Krittayavathananon, A., Luanwuthi, S., Srimuk, P., Nilmoung, S., ... & Limtrakul, J. (2014). Silver nanodendrite modified graphene rotating disk electrode for nonenzymatic hydrogen peroxide detection. *Carbon*, *70*, 287-294.
33. Fu, L., Lai, G., Mahon, P. J., Wang, J., Zhu, D., Jia, B., ... & Yu, A. (2014). Carbon nanotube and graphene oxide directed electrochemical synthesis of silver dendrites. *Rsc Advances*, *4*(75), 39645-39650.
34. Yang, Z., Tjiu, W. W., Fan, W., & Liu, T. (2013). Electrodepositing Ag nanodendrites on layered double hydroxides modified glassy carbon electrode: Novel hierarchical structure for hydrogen peroxide detection. *Electrochimica Acta*, *90*, 400-407.

35. Hu, J., Sun, J., Bian, C., Tong, J., & Shanhong, X. (2013). 3D Dendritic Nanostructure of Silver-Array: Preparation, Growth Mechanism and Application in Nitrate Sensor. *Electroanalysis*, *25*(2), 546-556.
36. Guadagnini, L., Ballarin, B., & Tonelli, D. (2013). Dendritic silver nanostructures obtained via one-step electrosynthesis: effect of nonanesulfonic acid and polyvinylpyrrolidone as additives on the analytical performance for hydrogen peroxide sensing. *Journal of nanoparticle research*, *15*(10), 1971.
37. Bian, J. C., Chen, Z. D., Li, Z., Yang, F., He, H. Y., Wang, J., ... & Han, G. R. (2012). Electrodeposition of hierarchical Ag nanostructures on ITO glass for reproducible and sensitive SERS application. *Applied Surface Science*, *258*(17), 6632-6636.
38. Bian, J., Li, Z., Chen, Z., Zhang, X., Li, Q., Jiang, S., ... & Han, G. (2012). Double-potentiostatic electrodeposition of Ag nanoflowers on ITO glass for reproducible surface-enhanced (resonance) Raman scattering application. *Electrochimica Acta*, *67*, 12-17.
39. Qin, X., Wang, H., Wang, X., Miao, Z., Fang, Y., Chen, Q., & Shao, X. (2011). Synthesis of dendritic silver nanostructures and their application in hydrogen peroxide electroreduction. *Electrochimica Acta*, *56*(9), 3170-3174.
40. Rezaei, B., & Damiri, S. (2010). Electrodeposited silver nanodendrites electrode with strongly enhanced electrocatalytic activity. *Talanta*, *83*(1), 197-204.
41. Zhang, J., Day, C. S., & Carroll, D. L. (2009). Controlled growth of novel hyper-branched nanostructures in nanoporous alumina membrane. *Chemical Communications*, (45), 6937-6939.
42. Jiang, Z., Lin, Y., & Xie, Z. (2012). Structural investigations and growth mechanism of well-defined Ag dendrites prepared by conventional redox displacement. *Materials Chemistry and Physics*, *134*(2-3), 762-767.

43. Ding, H. P., Xin, G. Q., Chen, K. C., Zhang, M., Liu, Q., Hao, J., & Liu, H. G. (2010). Silver dendritic nanostructures formed at the solid/liquid interface via electroless deposition. *Colloids and Surfaces A: Physicochemical and Engineering Aspects*, *353*(2-3), 166-171.
44. Fang, J., You, H., Kong, P., Yi, Y., Song, X., & Ding, B. (2007). Dendritic silver nanostructure growth and evolution in replacement reaction. *Crystal growth & design*, *7*(5), 864-867.
45. Feng, C., Zhao, Y., & Jiang, Y. (2015). Silver nano-dendritic crystal film: a rapid dehydration SERS substrate of totally new concept. *Rsc Advances*, *5*(6), 4578-4585.
46. Gu, H. X., Xue, L., Zhang, Y. F., Li, D. W., & Long, Y. T. (2015). Facile fabrication of a silver dendrite-integrated chip for surface-enhanced Raman scattering. *ACS applied materials & interfaces*, *7*(4), 2931-2936.
47. Zhang, Y., Sun, S., Zhang, X., Tang, L., Song, X., & Yang, Z. (2014). Sulfate-ion-assisted galvanic replacement tuning of silver dendrites to highly branched chains for effective SERS. *Physical Chemistry Chemical Physics*, *16*(35), 18918-18925.
48. Zhang, Y., Sun, S., Zhang, X., Tang, L., Song, X., Ding, B., & Yang, Z. (2014). Magnetic field controlled particle-mediated growth inducing icker-like silver architectures. *Chemical Engineering Journal*, *240*, 494-502.
49. Zhao, H., Wang, F., Ning, Y., Zhao, B., Yin, F., Lai, Y., ... & Zhang, D. (2013). Green “planting” nanostructured single crystal silver. *Scientific reports*, *3*, 1511.
50. Wang, F., Lai, Y., Zhao, B., Hu, X., Zhang, D., & Hu, K. (2010). Tunable growth of nanodendritic silver by galvanic-cell mechanism on formed activated carbon. *Chemical Communications*, *46*(21), 3782-3784.
51. Xu, J., Zhang, W., & Yang, Z. (2013). An optical humidity sensor based on Ag nanodendrites. *Applied Surface Science*, *280*, 920-925.

52. Avizienis, A. V., Martin-Olmos, C., Sillin, H. O., Aono, M., Gimzewski, J. K., & Stieg, A. Z. (2013). Morphological transitions from dendrites to nanowires in the electroless deposition of silver. *Crystal Growth & Design*, *13*(2), 465-469.
53. Cheng, W. M., Wang, C. C., & Chen, C. Y. (2012). The influence of Ni nanoparticles and Ni (II) on the growth of Ag dendrites immobilized on the chelating copolymer membrane. *Materials Chemistry and Physics*, *137*(1), 76-84.
54. Liu, R., Li, S., Yu, X., Zhang, G., Ma, Y., Yao, J., ... & Nadjo, L. (2011). Polyoxometalate-assisted galvanic replacement synthesis of silver hierarchical dendritic structures. *Crystal Growth & Design*, *11*(8), 3424-3431.
55. Hsiao, W. H., Chen, H. Y., Yang, Y. C., Chen, Y. L., Lee, C. Y., & Chiu, H. T. (2011). Surface-enhanced Raman scattering imaging of a single molecule on urchin-like silver nanowires. *ACS applied materials & interfaces*, *3*(9), 3280-3284.
56. Yang, Y., & Meng, G. (2010). Ag dendritic nanostructures for rapid detection of polychlorinated biphenyls based on surface-enhanced Raman scattering effect. *Journal of Applied Physics*, *107*(4), 044315.
57. Cheng, W. M., Wang, C. C., & Chen, C. Y. (2010). Preparing chelated copolymer membrane for fabrication of Ag dendrites. *Journal of colloid and interface science*, *348*(1), 49-56.
58. Ye, W., Shen, C., Tian, J., Wang, C., Hui, C., & Gao, H. (2009). Controllable growth of silver nanostructures by a simple replacement reaction and their SERS studies. *Solid State Sciences*, *11*(6), 1088-1093.
59. Ren, W., Guo, S., Dong, S., & Wang, E. (2011). A simple route for the synthesis of morphology-controlled and SERS-active Ag dendrites with near-infrared absorption. *The Journal of Physical Chemistry C*, *115*(21), 10315-10320.

60. Wang, L., Li, H., Tian, J., & Sun, X. (2010). Monodisperse, micrometer-scale, highly crystalline, nanotextured Ag dendrites: rapid, large-scale, wet-chemical synthesis and their application as SERS substrates. *ACS applied materials & interfaces*, *2*(11), 2987-2991.
61. Song, J., Hou, J., Tian, L., Guan, Y., Zhang, Y., & Zhu, X. X. (2015). Growth of giant silver dendrites on layer-by-layer assembled films. *Polymer*, *63*, 237-243.
62. Wang, Y., Camargo, P. H., Skrabalak, S. E., Gu, H., & Xia, Y. (2008). A facile, water-based synthesis of highly branched nanostructures of silver. *Langmuir*, *24*(20), 12042-12046.
63. Sun, X., & Hagner, M. (2007). Novel preparation of snowflake-like dendritic nanostructures of Ag or Au at room temperature via a wet-chemical route. *Langmuir*, *23*(18), 9147-9150.
64. Forati-Nezhad, M., Sadeghi, G. M. M., Yaghmaie, F., & Alimohammadi, F. (2015). Affecting the morphology of silver deposition on carbon nanotube surface: From nanoparticles to dendritic (tree-like) nanostructures. *Materials Science and Engineering: C*, *46*, 232-238.
65. Chen, Y. N., & Wang, H. (2015). Jellyfish mesoglea as a matrix for the synthesis of extremely high content silver dendrites. *Journal of colloid and interface science*, *454*, 14-19.
66. Yang, J., Cao, B., Li, H., & Liu, B. (2014). Investigation of the catalysis and SERS properties of flower-like and hierarchical silver microcrystals. *Journal of nanoparticle research*, *16*(10), 2651.
67. Sivakov, V., Kaniukov, E. Y., Petrov, A. V., Korolik, O. V., Mazanik, A. V., Bochmann, A., ... & Toimil-Molares, M. E. (2014). Silver nanostructures formation in porous Si/SiO2 matrix. *Journal of crystal growth*, *400*, 21-26.

68. Ng, C. H. B., & Fan, W. Y. (2014). Preparation of Ag stellar dendrites: modeling the growth of stellar snowflakes. *Crystal Growth & Design*, *14*(11), 6067-6072.
69. Alam, M. M., Ji, W., Luitel, H. N., Ozaki, Y., Watari, T., & Nakashima, K. (2014). Template free synthesis of dendritic silver nanostructures and their application in surface-enhanced Raman scattering. *Rsc Advances*, *4*(95), 52686-52689.
70. Wei, Y., Chen, Y., Ye, L., & Chang, P. (2011). Preparation of dendritic-like Ag crystals using monocrystalline silicon as template. *Materials Research Bulletin*, *46*(6), 929-936.
71. Keita, B., Brudna Holzle, L. R., Ngo Biboum, R., Nadjo, L., Mbomekalle, I. M., Franger, S., ... & Ekedi, G. A. (2011). Green wet chemical route for the synthesis of silver and palladium dendrites. *European Journal of Inorganic Chemistry*, *2011*(8), 1201-1204.
72. Mdluli, P. S., & Revaprasadu, N. (2009). Time dependant evolution of silver nanodendrites. *Materials Letters*, *63*(3-4), 447-450.
73. Laurier, K. G., Poets, M., Vermoortele, F., De Cremer, G., Martens, J. A., Uji-i, H., ... & Roeffaers, M. B. (2012). Photocatalytic growth of dendritic silver nanostructures as SERS substrates. *Chemical communications*, *48*(10), 1559-1561.
74. Ahmed, I., Wang, X., Boualili, N., Xu, H., Farha, R., Goldmann, M., & Ruhlmann, L. (2012). Photocatalytic synthesis of silver dendrites using electrostatic hybrid films of porphyrin–polyoxometalate. *Applied Catalysis A: General*, *447*, 89-99.
75. Wang, X., & Liu, X. (2011). Self-assembled synthesis of Ag nanodendrites and their applications to SERS. *Journal of Molecular Structure*, *997*(1-3), 64-69.
76. Qiao, Y., Lin, Y., Wang, Y., Li, Z., & Huang, J. (2011). Metal-driven viscoelastic wormlike micelle in anionic/zwitterionic surfactant systems and template-directed synthesis of dendritic silver nanostructures. *Langmuir*, *27*(5), 1718-1723.

77. Yang, C., Xie, Y. T., Yuen, M. M., Xiong, X., & Wong, C. P. (2010). A facile chemical approach for preparing a SERS active silver substrate. *Physical Chemistry Chemical Physics*, *12*(43), 14459-14461.
78. Tang, S., Meng, X., Lu, H., & Zhu, S. (2009). PVP-assisted sonoelectrochemical growth of silver nanostructures with various shapes. *Materials Chemistry and Physics*, *116*(2-3), 464-468.
79. Tang, S., Vongehr, S., & Meng, X. (2009). Two distinct branch–stem interfacial structures of silver dendrites with vertical and slanted branchings. *Chemical Physics Letters*, *477*(1-3), 179-183.
80. Zhu, J., Liu, S., Palchik, O., Koltypin, Y., & Gedanken, A. (2000). Shape-controlled synthesis of silver nanoparticles by pulse sonoelectrochemical methods. *Langmuir*, *16*(16), 6396-6399.
81. K. Kneipp, M. Moskovits and H. Kneipp, Surface-enhanced Raman Scattering-Physics and Applications, Top. Appl. Phys., 2006, 103
82. Zhou, Y., Yu, S. H., Wang, C. Y., Li, X. G., Zhu, Y. R., & Chen, Z. Y. (1999). A Novel ultraviolet irradiation photoreduction technique for the preparation of single-crystal Ag nanorods and Ag dendrites. *Advanced Materials*, *11*(10), 850-852.
83. Hahn, D. W. (2007). Raman scattering theory. *Department of Mechanical and Aerospace Engineering, University of Florida*.
84. M. Fleischman, P. J. Hendra, A. J. McQuilan: Chem. Phys. Lett. 26, 123 (1974)
85. Jeanmaire, D. L., & Van Duyne, R. P. (1977). Surface Raman spectroelectrochemistry: Part I. Heterocyclic, aromatic, and aliphatic amines adsorbed on the anodized silver electrode. *Journal of electroanalytical chemistry and interfacial electrochemistry*, *84*(1), 1-20.

86. Albrecht, M. G., & Creighton, J. A. (1977). Anomalously intense Raman spectra of pyridine at a silver electrode. *Journal of the american chemical society*, *99*(15), 5215-5217.
87. Moskovits, M. (1978). Surface roughness and the enhanced intensity of Raman scattering by molecules adsorbed on metals. *The Journal of Chemical Physics*, *69*(9), 4159-4161.
88. Kneipp, K., Kneipp, H., Itzkan, I., Dasari, R. R., & Feld, M. S. (1999). Ultrasensitive chemical analysis by Raman spectroscopy. *Chemical reviews*, *99*(10), 2957-2976.
89. Kneipp, K., Kneipp, H., Manoharan, R., Hanlon, E. B., Itzkan, I., Dasari, R. R., & Feld, M. S. (1998). Extremely large enhancement factors in surface-enhanced Raman scattering for molecules on colloidal gold clusters. *Applied spectroscopy*, *52*(12), 1493-1497.
90. Kneipp, K., Kneipp, H., Kartha, V. B., Manoharan, R., Deinum, G., Itzkan, I., ... & Feld, M. S. (1998). Detection and identification of a single DNA base molecule using surface-enhanced Raman scattering (SERS). *Physical Review E*, *57*(6), R6281.
91. Kneipp, K., Wang, Y., Kneipp, H., Perelman, L. T., Itzkan, I., Dasari, R. R., & Feld, M. S. (1997). Single molecule detection using surface-enhanced Raman scattering (SERS). *Physical review letters*, *78*(9), 1667.
92. Kneipp, K., Wang, Y., Kneipp, H., Itzkan, I., Dasari, R. R., & Feld, M. S. (1996). Population pumping of excited vibrational states by spontaneous surface-enhanced Raman scattering. *Physical review letters*, *76*(14), 2444.
93. Kneipp, K., Kneipp, H., Manoharan, R., Itzkan, I., Dasari, R. R., & Feld, M. S. (1998). Near-infrared surface-enhanced Raman scattering can detect single molecules and observe 'hot'vibrational transitions. *Journal of Raman Spectroscopy*, *29*(8), 743-747.

94. Krug, J. T., Wang, G. D., Emory, S. R., & Nie, S. (1999). Efficient Raman enhancement and intermittent light emission observed in single gold nanocrystals. *Journal of the American Chemical Society*, *121*(39), 9208-9214.

95. Emory, S. R., Haskins, W. E., & Nie, S. (1998). Direct observation of size-dependent optical enhancement in single metal nanoparticles. *Journal of the American Chemical Society*, *120*(31), 8009-8010.

96. Lyon, W. A., & Nie, S. (1997). Confinement and detection of single molecules in submicrometer channels. *Analytical Chemistry*, *69*(16), 3400-3405.

97. Nie, S., & Emory, S. R. (1997). Probing single molecules and single nanoparticles by surface-enhanced Raman scattering. *science*, *275*(5303), 1102-1106.

98. Doering, W. E., & Nie, S. (2002). Single-molecule and single-nanoparticle SERS: examining the roles of surface active sites and chemical enhancement. *The Journal of Physical Chemistry B*, *106*(2), 311-317.

99. Maxwell, D. J., Emory, S. R., & Nie, S. (2001). Nanostructured thin-film materials with surface-enhanced optical properties. *Chemistry of materials*, *13*(3), 1082-1088.

100. Gersten, J. I. (1980). The effect of surface roughness on surface enhanced Raman scattering. *The Journal of Chemical Physics*, *72*(10), 5779-5780.

101. Gersten, J. I. (1980). Rayleigh, Mie, and Raman scattering by molecules adsorbed on rough surfaces. The Journal of Chemical Physics, 72(10), 5780-5781.

102. Gersten, J., & Nitzan, A. (1980). Electromagnetic theory of enhanced Raman scattering by molecules adsorbed on rough surfaces. *The Journal of Chemical Physics*, *73*(7), 3023-3037.

103. Gersten, J., & Nitzan, A. (1981). Spectroscopic properties of molecules interacting with small dielectric particles. *The Journal of Chemical Physics*, *75*(3), 1139-1152.

104. McCall, S. L., & Platzman, P. M. (1980). Raman scattering from chemisorbed molecules at surfaces. *Physical Review B*, *22*(4), 1660.

105. McCall, S. L., Platzman, P. M., & Wolff, P. A. (1980). Surface enhanced Raman scattering. *Physics Letters A*, *77*(5), 381-383.

106. Kerker, M. (1979). Resonances in electromagnetic scattering by objects with negative absorption. *Applied Optics*, *18*(8), 1180-1189.

107. Kerker, M., Siiman, O., & Wang, D. S. (1984). Effect of aggregates on extinction and surface-enhanced Raman scattering spectra of colloidal silver. *The Journal of Physical Chemistry*, *88*(15), 3168-3170.

108. Wang, D. S., Kerker, M., & Chew, H. (1980). Surface enhanced Raman scattering (SERS) by molecules adsorbed at spherical particles: errata. *Appl. Opt.*, *19*, 4159.

109. Wang, D. S., & Kerker, M. (1981). Enhanced Raman scattering by molecules adsorbed at the surface of colloidal spheroids. *Physical Review B*, *24*(4), 1777.

110. Wang, D. S., & Kerker, M. (1982). Absorption and luminescence of dye-coated silver and gold particles. *Physical Review B*, *25*(4), 2433.

111. Moskovits, M. (1985). Surface-enhanced spectroscopy. *Reviews of modern physics*, *57*(3), 783.

112. J. D. Jackson: Electromagnetic Theory, 3rd ed. (Wiley, New York 1998)

113. Jensen, L., Aikens, C. M., & Schatz, G. C. (2008). Electronic structure methods for studying surface-enhanced Raman scattering. *Chemical Society Reviews*, *37*(5), 1061-1073.

114. Surface-Enhanced Raman Scattering. (n.d.). Retrieved May 14, 2017, from http://www.silmeco.com/knowledge-base/surface-enhanced-raman-scattering/

115. U. Kreibig, C. Von Frags: Z. Physik 224, 307 (1969)

116. Kreibig, U., & Zacharias, P. (1970). Surface plasma resonances in small spherical silver and gold particles. *Zeitschrift für Physik A Hadrons and nuclei*, *231*(2), 128-143.

117. Dignam, M. J., & Moskovits, M. (1973). Optical properties of sub-monolayer molecular films. *Journal of the Chemical Society, Faraday Transactions 2: Molecular and Chemical Physics*, *69*, 56-64.

118. Kelf, T. A., Sugawara, Y., Baumberg, J. J., Abdelsalam, M., & Bartlett, P. N. (2005). Plasmonic band gaps and trapped plasmons on nanostructured metal surfaces. *Physical review letters*, *95*(11), 116802.

119. Baumberg, J. J., Kelf, T. A., Sugawara, Y., Cintra, S., Abdelsalam, M. E., Bartlett, P. N., & Russell, A. E. (2005). Angle-resolved surface-enhanced Raman scattering on metallic nanostructured plasmonic crystals. *Nano letters*, *5*(11), 2262-2267.

120. Perney, N. M., Baumberg, J. J., Zoorob, M. E., Charlton, M. D., Mahnkopf, S., & Netti, C. M. (2006). Tuning localized plasmons in nanostructured substrates for surface-enhanced Raman scattering. *Optics express*, *14*(2), 847-857.

121. Aravind, 1., Nitzan, A., & Metiu, H. (1981). The interaction between electromagnetic resonances and its role in spectroscopic studies of molecules adsorbed on colloidal particles or metal spheres. *Surface Science*, *110*(1), 189-204.

122. Aravind, P. K., & Metiu, H. (1982). Use of a perfectly conducting sphere to excite the plasmon of a flat surface. 1. Calculation of the local field with applications to surface-enhanced spectroscopy. *The Journal of Physical Chemistry*, *86*(26), 5076-5084.

123. Aravind, P. K., & Metiu, H. (1983). The effects of the interaction between resonances in the electromagnetic response of a sphere-plane structure; applications to surface enhanced spectroscopy. *Surface science*, *124*(2-3), 506-528.

124. Liver, N., Nitzan, A., & Gersten, J. I. (1984). Local fields in cavity sites of rough dielectric surfaces. *Chemical physics letters*, *111*(4-5), 449-454.

125. Griess test. (2017, March 23). Retrieved May 15, 2017, from https://en.wikipedia.org/wiki/Griess_test

126. Han, Y., Liu, S., Han, M., Bao, J., & Dai, Z. (2009). Fabrication of hierarchical nanostructure of silver via a surfactant-free mixed solvents route. *Crystal Growth and Design*, *9*(9), 3941-3947.

127. Penn, R. L., & Banfield, J. F. (1998). Imperfect oriented attachment: dislocation generation in defect-free nanocrystals. *Science*, *281*(5379), 969-971.

128. Washio, I., Xiong, Y., Yin, Y., & Xia, Y. (2006). Reduction by the end groups of poly (vinyl pyrrolidone): a new and versatile route to the kinetically controlled synthesis of Ag triangular nanoplates. *Advanced Materials*, *18*(13), 1745-1749.

129. Yang, S., Dai, X., Stogin, B. B., & Wong, T. S. (2016). Ultrasensitive surface-enhanced Raman scattering detection in common fluids. *Proceedings of the National Academy of Sciences*, *113*(2), 268-273.

130. Hildebrandt, P., & Stockburger, M. (1984). Surface-enhanced resonance Raman spectroscopy of Rhodamine 6G adsorbed on colloidal silver. *The Journal of Physical Chemistry*, *88*(24), 5935-5944.

131. Moskovits M. (2006) Surface-Enhanced Raman Spectroscopy: a Brief Perspective. In: Kneipp K., Moskovits M., Kneipp H. (eds) Surface-Enhanced Raman Scattering. Topics in Applied Physics, vol 103. Springer, Berlin, Heidelberg

132. Leng, Y. (2010). Vibrational Spectroscopy for Molecular Analysis. In Materials Characterization, Y. Leng (Ed.). doi:10.1002/9780470823002.ch9

Biographical Information

Milind Mansing Pawar was born in Vadodara in state of Gujarat, India. He received his B.E in Metallurgical and Materials Engineering from the Maharaja Sayajirao University of Baroda, Vadodara, India. Milind is a Master's thesis research student at University of Texas at Arlington in Department of Materials Science and Engineering. He is a member of Dr. Hao's research group and an active member of American Society of Materials (ASM) UTA student chapter. His research is associated with development of nanostructures for its real-world application. Milind has hands on experience with Raman spectroscopy, Scanning electron microscopy and XRD.